AFRL-SR-AR-TR-06-0017

REPORT DOCUMENTATION PAGE

1. AGENCY USE ONLY (Leave blank)	2. REPORT DATE	3. REPORT TYPE AND DATES COVERED
	11-01-2006	Final Performance, 01-12-02 to 31-12-05

4. TITLE AND SUBTITLE
The analysis and modeling of phase stability and multiphase designs in high temperature refractory metal-silicon-boron alloys

5. FUNDING NUMBERS
F49620-03-1-0033

6. AUTHOR(S)
Professor John H. Perepezko

7. PERFORMING ORGANIZATION NAME(S) AND ADDRESS(ES)
University of Wisconsin-Madison
Research Administration
750 University Ave.
Madison, WI 53706

8. PERFORMING ORGANIZATION REPORT NUMBER

9. SPONSORING / MONITORING AGENCY NAME(S) AND ADDRESS(ES)
AF Office of Scientific Research
Research/NA (Dr.J. Tiley)
Metallic Materials
801 N. Randolph Street
Arlington, VA 22203

10. SPONSORING / MONITORING AGENCY REPORT NUMBER

11. SUPPLEMENTARY NOTES

12a. DISTRIBUTION / AVAILABILITY STATEMENT
Approved for public release,
distribution unlimited

12b. DISTRIBUTION CODE

13. ABSTRACT *(Maximum 200 Words)*

In order to satisfy the challenging materials requirements for operation in a high temperature (T>1400°C) environment, multiphase alloy microstructures in the Mo-Si-B system involving the Mo_5SiB_2 (T_2) intermetallic phase have been identified that offer high melting temperature, oxidation resistance and attractive high temperature mechanical properties. With the T_2 phase as the focal point of the microstructure designs, the fundamental basis of the alloying behavior in T_2 has been established in terms of the governing geometric and electronic factors. For non-stoichiometric compositions, it has been determined that constitutional defects such as vacancies for Mo-rich compositions and anti-site defects for Mo-lean compositions control the homogeneity range. Moreover, the aggregation of constitutional vacancies has been discovered to play a key role in the development of dislocation and precipitation reactions in the T_2 phase that directly impact high temperature structural performance. To establish the essential database for computational modeling, an experimental campaign has been pursued in the current work to measure high temperature solubility up to 1950°C, to quantify sluggish diffusion and to characterize the defect structure in the T_2 phase.

14. SUBJECT TERMS	15. NUMBER OF PAGES
High Temperature Alloys, Refractory Metals, Phase Stability, Diffusion, Multiphase Microstructure	43
	16. PRICE CODE

17. SECURITY CLASSIFICATION OF REPORT	18. SECURITY CLASSIFICATION OF THIS PAGE	19. SECURITY CLASSIFICATION OF ABSTRACT	20. LIMITATION OF ABSTRACT

NSN 7540-01-280-5500

Standard Form 298 (Rev. 2-89)
Prescribed by ANSI Std. Z39-18

TABLE OF CONTENTS

1. Introduction

The challenges of a high temperature environment (T>1400°C) impose severe material performance constraints in terms of melting point, oxidation resistance and structural functionality. A number of ceramic materials, intermetallic compounds and refractory metals with high melting temperature are available as material choices. However, in a single component, single phase form, these materials rarely satisfy all the above requirements because of the brittleness of ceramic materials and intermetallic compounds at low temperatures and the oxidation problems and poor creep resistance of refractory metals at high temperatures. In this respect the evolutionary development of high temperature alloys over the past 4-5 decades represents a remarkable achievement and provides important lessons to guide future materials design efforts. One clear message is the importance of multiphase microstructures and the capability to control phase fractions and morphologies within the overall structure [87Sto,87Ros,90Dys]. The flexibility in microstructure control has been shown to be critical in tailoring alloy performance in order to satisfy a number of mechanical property requirements that sometimes present conflicting demands [92Dim,91Kim]. Besides the essential structural requirements, elevated temperatures also often involve aggressive environments that require a material to display an inherent oxidation protection that can be enhanced further by coating [79Mai].

In terms of metallic system candidates there are several high melting temperature intermetallics, but there is a much smaller number of intermetallic phases that offer a level of inherent environmental resistance. At elevated temperature, alloy phases that contain Al or Si are most attractive for developing stable Al_2O_3 and SiO_2 coatings. Moreover, above about 1300°C, SiO_2 films are preferred since the parabolic rate constant for oxidation is lower for SiO_2 than for Al_2O_3 [83Bir]. In fact, this selection is supported by the superior oxidation resistance available with monolithic $MoSi_2$ where a SiO_2 surface provides for useful operation up to about 1700°C (i.e. 0.8 T_m). At high temperatures the creep strength of $MoSi_2$ is insufficient and at low temperature it is brittle [92Vas,92Sha,92Boe].

At the same time, the multiphase microstructures that can be developed in the Mo-Si-B system involving the high melting temperature (>2100°C) ternary-based intermetallic Mo_5SiB_2 (T_2) offer an attractive option particularly due to the superior oxidation resistance of the Mo-based silicides [97Per,97Nun]. In terms of the available phase combinations in the Mo-Si-B system, the two-phase combination of Mo(ss)+T_2 offers enhanced toughening [00Nun] due to a precipitation of Mo(ss) that can be produced within the T_2 phase [98Sak,99Sak,99Sch] while three phase alloys comprised of Mo(ss), T_2 and Mo_3Si or Mo_3Si, T_2 and Mo_5Si_3 offer favorable oxidation resistance [99Sch,98Sch,93Tho]. A focal point of the microstructural designs is clearly the T_2 phase that is central to the phase selections that promote high temperature stability and robust microstructures. In this regard, a comprehensive assessment of the solidification behavior is critical as well since the solidification structure ultimately plays a key role in the morphological control of the microstructure. The T_2 phase develops upon solidification through a peritectic reaction and exhibits a range of solubility [00Nun]. Consequently, constitutional defects must be introduced to accommodate non-stoichiometric compositions. In ternary alloys direct formation of Mo+T_2 structures is not possible due to severe segregation under usual solidification processing conditions [99Sak2]. Rapid solidification processing such that available in powders is effective in suppressing the solidification segregation [97Per,99Sak2]. However, alternate approaches are also of interest for bulk ingots. For example, selected refractory

metal substitutional alloying, such as the incorporation of Nb to alter the solubility of the T_2 phase and the relative phase stability has been shown to be an effective method to control the solidification of two phase refractory solid solution + T_2 structures [00Sak]. The observed alloying trends also highlight the fundamental factors related to the defect structure and atomic size factor that influence the relative stability of the T_2 phase and provide a basis to develop a thermodynamic model of the phase equilibria. Coupled with the thermodynamic predictions, the synergy of phase stability and solidification control will be a critical prerequisite for further microstructure developments.

It is appropriate to consider briefly some of the contemporary approaches to developing phase stability models in complex multicomponent multiphase systems. Indeed this major task has been a challenge for some time. However, a variety of approaches have evolved that have made useful contributions to the understanding in simpler systems, but also reveal some limitations. For example, electronic structure calculations have been advanced by the use of density-functional theory (DFT) as a many-body approach and the application of the local density approximation (LDA). By simplifying the DFT problem to treat valence electrons under the assumption that the core electrons experience little change due to the chemical reactions, further advancement has been achieved by the introduction of the plane-wave pseudopotential (PW-PP) technique [00Alf]. This approach has enabled the band structures as well as other physical properties of the transition metals, in particular, to be elucidated. Moreover, the use of Debye model which incorporates the phonon contribution to the elastic response has been successful in examining refractory silicides that typically exhibit a strong p-d hybridization with correspondingly high optical phonon energies. Fu et. al. for example have been able to analyze the thermoelastic characteristics of the refractory silicides including the T_2 and T_1 phases and pointed to the source of the large coefficient of thermal expansion (CTE) anisotropy in the T_1 phase as due to a high lattice anharmonicity in the <001> direction and a elastically stiff basal plane [00Fu]. Furthermore, the calculation is also consistent with the more isotropic behavior of the CTE in the T_2 phase since the short Mo-Mo chains in the T_1 phase are not present in the T_2 phase. Overall, the first principle types of calculations give useful estimates of the ground state behavior and the low temperature relative phase stability. In fact, the calculated energies for different stoichiometric reference structures are often in reasonable agreement with the lattice stabilities evaluated by thermodynamic analysis [00Alf]. However, a complete description of the relative phase stability over a wide range of temperature and composition with the inclusion of constitutional defects and phase transitions remains a challenge and a limitation to providing the necessary guidance for effective multiphase designs in structural applications.

At the same time, when considering a system for the first time, it is necessary to have a baseline of phase stability knowledge before attempting any model development. In fact, as the database grows, the level of modeling can also evolve, but an initial effort can offer significant benefit if it maintains a contact with the database in order to minimize the number of limiting assumptions. For this purpose, a computational thermodynamic model in the spirit of the CALPHAD approach is proposed since it provides an effective basis for the interpolation of results as well as for the extrapolation of behavior outside of the database to give predictive guidance.

The central theme in this proposal is to coordinate a comprehensive approach involving joint experimental and modeling work that integrates multiphase stability concepts and models to provide insight into the control of solidification and multiphase reactions to guide the design of high temperature T_2-based microstructures and alloy

compositions. The examination of multiphase stability centering on the T_2 phase will incorporate a careful determination of the defect structure mechanisms that control the phase stability. TEM studies will provide an analysis of dislocation structures. Similarly, a parallel effort will be devoted to examine the changes in T_2 phase stability with refractory metal and metalloid substitution. These critical experimental observations will enable the formulation of a comprehensive thermodynamic modeling of the stability of the T_2 phase as well as the multiphase configurations involving the T_2 phase.

2. Research Highlights

2.1. Phase Stability in the Mo-rich Mo-Si-B System at Various Temperatures

Building on our prior work where the liquidus projection [97Nun], a schematic Mo-T_2 plethal section and the phase diagram isotherm of the Mo-rich Mo-Si-B system at 1600 °C [00Per] have been established the phase diagram isotherms for the Mo-rich portion of the Mo-Si-B system have been determined at various high temperatures (≥1600°C) as shown in figure 1. Three-phase samples such as: [Mo(ss)-T_2-Mo_2B], [Mo_2B-T_2-MoB], [MoB-T_2-Mo_5Si_3], [Mo_5Si_3–T_2-Mo_3Si] and [Mo_3Si-T_2-Mo(ss)] were equilibrated in a high-temperature furnace in range of 1600 – 1950 °C under high vacuum. The EPMA examination on three-phase equilibrium samples allowed the determination of phase identities and the phase boundary compositions. Various Si and B solubilities of Mo(ss), Mo_2B, MoB, Mo_3Si, Mo_5Si_3 and T_2 as a function of temperature is shown in figure x1, where each column contains Si and B solubility diagrams for a phase existing in three-phase samples and three phases in the three-phase sample is described at the bottom of each column. For example, first column includes the Si and B solubility diagrams of Mo(ss), Mo_2B and T_2 in the [Mo(ss)-T_2-Mo_2B] three-phase sample. Fitting the Si and B solubility data in figure x1 led to the relationships between solubility and temperature. Based on these relationship, table 1 exhibits the Si and B solubility limits of Mo(ss), molybdenum silicides and molybdenum borides in the Mo-rich Mo-Si-B system at 1600, 1870 and 1950 °C. As temperature increases from 1600 °C to 1950 °C, the highest Si and B solubility limits of Mo(ss) increase from 2.91 at%Si to 6.08 at%Si, and 0 at%B to 1.29 at%B, respectively. Boundary compositions of Mo_2B at the Mo(ss)+Mo_2B/Mo_2B and Mo_2B/Mo_2B+MoB phase field boundaries shift towards the Mo-rich side with increasing temperature. The Si and B solubility limits of MoB and Mo_5Si_3, as shown in table 1, were determined from EPMA measurements on three-phase samples such as [Mo_2B-T_2-MoB], [MoB-T_2-Mo_5Si3] and [Mo_5Si_3-T_2-Mo_3Si]. Table 1 also shows that the boundary composition of MoB at the Mo_2B+MoB/MoB phase field boundary shifts towards the Mo-rich side with increasing temperature. Molybdenum boride phases (Mo_2B and MoB) have negligible Si solubility at 1600 °C, but their Si solubility limits increase with increasing temperature. Negligible B solubility in table 1 indicates that boron is insoluble in molybdenum silicide phases (Mo_3Si and Mo_5Si_3) at 1600 – 1950 °C. In addition, the Si solubility limit of Mo_3Si on the Mo-rich side at 1950 °C is not displayed, because a three-phase sample [Mo(ss)+T_2+Mo_3Si] melted above 1870 °C. This elucidates that three, three-phase equilibria such as [Mo(ss)+L+T_2], [T_2+L+Mo_3Si] and [Mo_3Si+L+Mo(ss)] are formed above 1870 °C (dotted lines in figure 1(c)). The phase stability analyses on the Mo-rich Mo-Si-B system in temperature range of

1600-1950 °C revealed that Mo_3Si and Mo_5Si_3 exhibit no B solubility, and MoB exhibits no Si solubility, while Mo_2B exhibits no Si solubility at 1600 °C but appreciable Si solubility at 1950 °C. Moreover, the thermodynamic model for Mo_2B has excluded Si occupancy on either the Mo or B sublattice sites, because the thermodynamic model was attributed to the phase stability of Mo-rich Mo-Si-B system at 1600 °C [05Yan,05Yan2]. This indicates that the thermodynamic model for Mo_2B has to be modified to contain Si solubility.

The homogeneity range changes of the T_2 phase with the increasing temperature are shown in figure 1(d). In the Mo(ss)-T_2-Mo_2B three-phase equilibrium region the T_2 boundary composition shifts towards the Mo(ss) solid solution phase (richer Mo, less Si, and less B) with increasing temperature. The T_2 phase in equilibrium with Mo(ss) and Mo_2B exhibits higher Mo solubility limit, leading to Mo supersaturation of T_2 in a Mo(ss)+T_2 alloy. The Mo supersaturated T_2 phase precipitates Mo, as previously observed (figure 2). Due to the larger size of a Mo atom compared to Si and B atoms, the Mo concentration in excess of stoichiometry forms constitutional vacancies as a defect. In the Mo_3Si-T_2-Mo(ss) three-phase equilibrium region, as temperature increases, the T_2 boundary composition displaces in a direction where the B and Si solubilities decrease and the Mo solubility slightly increases. Displacement behavior of two three-phase equilibrium regions (Mo(ss)+T_2+Mo_2B and Mo(ss)+T_2+Mo_3Si) as a function of temperature indicates that the phase field boundary between T_2 and T_2+Mo(ss) extends towards the Mo(ss) side as temperature increases. In other words, the Mo solubility limit of the T_2 phase in a Mo(ss)+T_2 alloy increases with temperature, which yields an increasing constitutional vacancy content in the T_2 structure. For instance, when a Mo(ss)+T_2 alloy is homogenized at a high temperature and quenched to a lower temperature, it has an excess of Mo in T_2. The annealing process promotes the formation of Mo precipitates in T_2 as evidenced in figure 2. Mo precipitation is accompanied by the aggregation of constitutional vacancies that would be the source for formation of a dislocation loop (see the later section). In the Mo_2B-T_2-MoB three-phase equilibrium region, as temperature increases, the T_2 boundary composition displaces in a direction where the B solubility decreases and the Mo solubility increases while the Si solubility remains approximately constant. The anti-site B substitution over the Mo sublattice sites appears to decrease. Shifting the phase field boundary between the T_2 phase field and T_2+MoB two-phase field away from the MoB side does not allow B supersaturation of the T_2 phase in a quenched Mo_2B+T_2 alloy. In the MoB-T_2-Mo_5Si_3 three-phase equilibrium region, as temperature increases, the T_2 boundary composition displaces in a direction where the B solubility decreases and the Si solubility increases while the Mo solubility approximately remains constant. The anti-site substitution between the Si and B sublattice sites appears to occur. Si supersaturation occurs in the T_2 phase in a quenched MoB-T_2-T_1 alloy, but the phase field boundary between T_2 and T_2+T_1 is displaced little with increasing temperature. In the Mo_5Si_3-T_2-Mo_3Si three-phase equilibrium region, as temperature increases, the T_2 boundary composition displaces in a direction where the B solubility decreases and the Mo solubility increases while the Si solubility remains approximately constant. Mo supersaturation can occur in the quenched T_2 phase.

The new information on the phase stability of the Mo-rich Mo-Si-B system at various temperatures (≥ 1600 °C), provides a basis to update the isoplethal section between Mo and T_2. Figure 3 shows (a) previously reported isoplethal section between Mo-T_2 [97Nun] and (b) the updated isoplethal section between Mo-T_2. Previously, the isoplethal section (figure 3(a)) exhibited that there is no phase field except Mo(ss)+T_2 below 2100 °C. However, the

present study of phase stability changes of the Mo-rich Mo-Si-B system with the increasing temperatures indicates that below 2100 °C there exist two single-phase fields (Mo(ss) and T_2), three two-phase fields (Mo(ss)+Mo_2B, Mo(ss)+T_2, and L+T_2), and two three-phase fields (Mo(ss)+Mo_2B+T_2 and L+Mo_2B+T_2), as shown in figure 3(b). Also, the volume fraction changes of the three-phase equilibrium alloy sample with the changing temperature are established using known phase densities. Figure 4 illustrates the volume fraction changes of the $Mo_{85}Si_{10}B_5$ alloy that consists of Mo(ss), T_2 and A15(Mo_3Si). As the temperature increases, volume fraction of Mo(ss) increases and volume fraction of A15 decreases while volume fraction of T_2 remains constant. This indicates that managing initial nominal composition of a three-phase equilibrium alloy can be used to control the constituent phase volume fractions.

2.2. Annealing Response of Constitutional Vacancies and Dislocation in T_2 phase

It is evident from the systematic investigations on the phase equilibria and solidification pathways for the Mo-rich portion in the Mo-Si-B ternary system [97Nun,00Nun,01Kim] that the ternary Mo_5SiB_2 (T_2) phase is the key constituent and exhibits a distinct range of homogeneity around the stoichiometric composition. The constitutional vacancy has been proposed as a defect mechanism to explain the dependence of the lattice parameters on the T_2 phase composition [97Nun]. The T_2 phase has also been found to exhibit temperature dependent solubility, which is manifested by the Mo(ss) precipitation reaction upon annealing [97Nun,99Sak]. The Mo(ss) precipitation, however, can be observed only in the Mo(ss)/T_2 two-phase alloys, and the T_2 phase solubilities associated with the other phase regions exhibit smaller changes with temperature variations. Moreover, small Nb additions to a Mo(ss)/T_2 two-phase alloy inhibit the formation of Mo(ss) precipitates in T_2 phase. Namely, the stability of T_2 phase is strongly related to constitutional defects, and the elucidation of constitutional defect mechanism is critical to understanding the stability of the T_2 phase. In the present study a TEM analysis was conducted to reveal the T_2 phase substructure changes upon annealing, as well as the defect structures in T_2 phase [05Sek].

As depicted in figure 5, the as-cast microstructure of a Mo-10Si-20B alloy consists of three phases: Mo(ss), A15, and T_2. The primary solidification phase is a faceted T_2 phase, and the Mo(ss)/T_2 mono-variant eutectic products have formed to enclose the T_2 primary, followed by the formation of Mo(ss)/T_2/A15 three-phase microstructure as the final solidification product. After the annealing of the alloy at 1600 °C for 150 hours, Mo(ss) particles have precipitated in the primary T_2 matrix. TEM observations have revealed that the dislocation density in the primary T_2 phase increases with annealing time. Few dislocations and no precipitates are present in the T_2 primary of an as-cast alloy, while many dislocations have developed in the T_2 phase of the alloy annealed at 1550 °C for 20 hours. At the same time, it is also evident that the plate shaped Mo(ss) particles have preferentially precipitated on these dislocations. Considering that these dislocations have developed only by annealing, and the homogeneity range of T_2 phase is attributed to the introduction of constitutional defects [97Nun], it is possible that these dislocations are formed by the removal of excess constitutional vacancies during annealing. This fact is supported by the lattice parameter variation by annealing time; the volume of the T_2 unit cell increases with annealing time, although larger sized excess Mo atoms are eliminated to form the Mo(ss) precipitates during

annealing, as shown in table 2. It is therefore concluded that excess vacancies introduced during solidification in T_2 phase are removed to form dislocations upon annealing, which then provide the heterogeneous nucleation sites for the subsequent (Mo) precipitation.

The dislocations are analyzed by the thickness fringe method [80Ish], which can uniquely determine the Burgers vectors of dislocations by counting the number of thickness fringes terminated at the end of each dislocation imaged in weak-beam mode under three different reflection vectors. Selected micrographs are shown in figure 6, in which the Burgers vector of dislocation is determined as [110]. By a combination of Burgers vector and dislocation line vector analyses, the dislocation network formed in the T_2 phase of the annealed Mo-10Si-20B alloy is characterized as shown in figure. 7. The dislocation network consists of edge dislocations: the Burgers vectors of the dislocations with line vectors of <100], <110], and <001] are <100], <110], and <100] types, respectively. According to the anisotropic elasticity theory, the line energy per unit length of a dislocation, E, is given by [82Hir]:

$$E = \left(\frac{Kb^2}{4\pi}\right)\ln\left(\frac{R}{r_0}\right) \qquad [1]$$

, where b is the magnitude of the Burgers vector, R/r_0 is the ratio of the outer and inner cut-off radii in the continuum description of dislocations, and K is the energy factor which is a function of the elastic constants of the crystal and the line direction of a dislocation. For the calculations, the elastic constants determined by Ihara et al. [02Iha] are used, and the R/r_0 term is tentatively kept as $\exp(4\pi)$, by which the dislocation line energy is simply given by $E = Kb^2$. The calculated energy factors and dislocation line energies for some possible dislocations are shown in table 3. The dislocation network observed in the present study consists of mostly edge dislocations, although the line energies of screw dislocations are much smaller than those of edge dislocations. The excessive development of edge segments supports the fact that the dislocations formed in the T_2 phase are originated from an agglomeration of excess vacancies during annealing, since a prismatic loop forms when excess vacancies are attracted and collapsed into a dislocation. Field et al. have examined possible slip systems in T_2 phase based on the crystallography and energetic factors, and found that two slip system, <100]/{001) and 1/2<111]/{112) are favored over any other slip systems [01Fie]. These two slip directions are consistent with the two smallest lattice translation vectors in the T_2 crystal, and would be reasonable from a dislocation line energy point of view, as depicted in table 3. However in the present study, many <110] dislocations, of which line energies are about twice as large as those of <100] dislocations, have developed by vacancy agglomeration during annealing. This fact may indicate that the preference of dislocation development by excess vacancy attraction is different to that induced by deformations. It should be noted that although the mobility of prismatic dislocations is intrinsically low, these dislocations could act as Frank-Read sources under suitable external stresses, and therefore enhance the deformability at high temperatures.

2.3. Kinetic Behavior in the Mo_2B/Mo_5Si_3 Diffusion Couples

To investigate the diffusion kinetics in the T_2 phase that is associated with atom movements that influence microstructure morphology, phase transformation, growth rate, and phase stability, a Mo_2B/Mo_5Si_3 diffusion couple

has been used for determining the diffusion coefficients. Annealing the Mo_2B/Mo_5Si_3 diffusion couple generally developed the T_2 and Mo_3Si phases in the diffusion zone between Mo_2B and Mo_5Si_3, which yielded the $Mo_2B/T_2/Mo_3Si/Mo_5Si_3$ (figure 8) diffusion pathway. In the Mo_2B/Mo_5Si_3 diffusion couple annealed at 1600 °C for 400 hours the distinct diffusion pathway was observed to be $Mo_2B/T_2/Mo_5Si_3$. Figure 8(b) shows both the $Mo_2B/T_2/Mo_5Si_3$ and $Mo_2B/T_2/Mo_3Si/Mo_5Si_3$ diffusion pathways that were observed in the Mo_2B/Mo_5Si_3 diffusion couple annealed at 1600 °C for 805 hours. In the latter diffusion pathway (figure 8(b)), the Mo_3Si phase was observed in a few local regions at the T_2/Mo_5Si_3 interface. The measured thickness of the Mo_3Si and T_2 phases is plotted in figure 9(a,b). The Mo_3Si phase exhibits a maximum in layer growth thickness with a peak that occurs at earlier annealing time as the annealing temperature increases, while the T_2 phase continuously grows with time. The disappearance of Mo_3Si at long-term heat treatment (figure 8(b)) indicates that the $Mo_2B/T_2/Mo_3Si/Mo_5Si_3$ diffusion pathway is not a steady state path, but reflects transient conditions. The $Mo_2B/T_2/Mo_5Si_3$ diffusion pathway may be a stable path. The T_2 layer thickness was measured in diffusion couples annealed at various temperatures and times. The parabolic kinetics fit in figure 9(a) was used to determine the layer growth constant k at each temperature [85Atk]. A plot of the rate constant versus reciprocal temperature (figure 10) allows for a determination of the activation energy for growth of the T_2 phase as 278.8 kJ/mol.

Concentration profiles of Si and B (figure 11) were obtained from EPMA measurements over the diffusion reaction zone between Mo_2B and Mo_5Si_3. Dayananda [96Ddy] developed an analysis method to determine the interdiffusion coefficients from single diffusion couple experiment in a multicomponent system. He introduced relationships between the average interdiffusion coefficients and the interdiffusion flux:

$$\frac{\int_{C_i^+}^{C_i^0}(x-x_0)^2\,dC_i}{2t(C_i^0-C_i^+)} = \overline{\widetilde{D}_{ii}^n} + \overline{\widetilde{D}_{ij}^n}\frac{(C_j^+-C_j^0)}{(C_i^+-C_i^0)} \text{ and } \frac{\int_{C_i^0}^{C_i^-}(x-x_0)^2\,dC_i}{2t(C_i^--C_i^0)} = \overline{\widetilde{D}_{ii}^n} + \overline{\widetilde{D}_{ij}^n}\frac{(C_j^0-C_j^-)}{(C_i^0-C_i^-)} \qquad [2]$$

where $(x-x_0)$ is relative distance with respect to the Matano plane at $x=x_0$, and t is annealing time. C_i^0 C_i^+ and C_i^- are concentrations of component i at $x=x_0$, $x=+\infty$, and $x=-\infty$, respectively. $\overline{\widetilde{D}_{ii}^n}$ and $\overline{\widetilde{D}_{ij}^n}$ are the average interdiffusion coefficients over the selected composition range of the diffusion zone. In a multicomponent system, the flux of a component depends on its own concentration gradient as well as on the concentration gradient of all other components in the system. According to the Fick's first law,

$$J_i = \sum_j^{n-1} \widetilde{D}_{ij}^n \nabla C_j \qquad [3]$$

where J_i is the flux of component i, $\widetilde{D}_{ij}^n$ is the interdiffusion coefficient, and ∇C_j is the concentration gradient of component j. The diffusivity matrix that is an $(n\text{-}1)\times(n\text{-}1)$ square matrix in an n-component system can fully describe the dependence of a diffusion flux on the concentration gradient of all the components. In this regard, a diffusion flux in the Mo-Si-B ternary system depends on only four independent interdiffusion coefficients. Based on the above equation [2] proposed by Dayananda, four independent average interdiffusion coefficients can be estimated that is shown in figure 12. The T_2 phase developed in the Mo_2B/Mo_5Si_3 diffusion couple exhibits small concentration changes of Si and B ($\leq$ 2 at%), indicating that the interdiffusion coefficients can be approximately

constant. Subsequently, the estimated average interdiffusion coefficients can be regarded as the interdiffusion coefficients of the T_2 phase. The estimated values of $\tilde{D}^{Mo}_{SiSi}$ and $\tilde{D}^{Mo}_{SiB}$ are positive, but $\tilde{D}^{Mo}_{BSi}$ and $\tilde{D}^{Mo}_{BB}$ exhibit negative values. Positive $\tilde{D}^{Mo}_{SiSi}$ and $\tilde{D}^{Mo}_{SiB}$ values indicate that the Si concentration gradient drives Si atoms to flow in a direction of decreasing Si concentration, while the B concentration gradient drives Si atoms to flow in an opposite direction. The Si concentration profile (figure 11) shows that the Si net flow occurs in the direction of negative Si concentration gradient. This indicates that the Si concentration gradient as a driving force plays a key role in Si atom movements. Negative $\tilde{D}^{Mo}_{BSi}$ and $\tilde{D}^{Mo}_{BB}$ elucidates that the Si concentration gradient drives B atoms to flow in a direction that the Si concentration increases, and the B concentration gradient makes B atoms to flow in a direction that the B concentration increases. The B concentration profile (figure 11) shows that the B net flow occurs in the direction of positive B concentration gradient. This indicates that the Si concentration gradient as a driving force also plays a key role in B atom movements. Consequently, the Si and B diffusion behaviors reflect that Si and B atom movements in the T_2 phase are coupled and mainly controlled by the Si concentration gradient driving force.

As noted in figures 12 (a-d) the activation energy for interdiffusion, Q, is in the range of 300 – 360 kJ/mol. The activation energy for the T_2 phase layer growth (figure 11) is notably lower than the estimated activation energies for interdiffusion (figure 12) that are 358.1 kJ/mol relevant to $\tilde{D}^{Mo}_{SiSi}$, 348.0 kJ/mol to $\tilde{D}^{Mo}_{SiB}$, 304.6 kJ/mol to $\tilde{D}^{Mo}_{BSi}$, and 303.9 kJ/mol to $\tilde{D}^{Mo}_{BB}$. In comparison, Tortorici *et al.* [99Tor] studied interdiffusion of the $MoSi_2$ and Mo_5Si_3 phase layers developed in the Mo/Si diffusion couples annealed at 900 – 1350 °C, where the activation energy for interdiffusion of $MoSi_2$ is 130 ± 20 kJ/mol and that of Mo_5Si_3 is 210 ± 10 kJ/mol. Their estimated average interdiffusion coefficient for the $MoSi_2$ phase is 2.2 - 2.4 × 10^{-8} cm^2/s at 1350 °C. Hayashi et al. [05Hay] recently reported that the activation energy for the Mo_5Si_3 layer growth in the $MoSi_2/T_2$ diffusion couple is 310 kJ/mol. The average interdiffusion coefficient for Mo_5Si_3 is 4.1 × 10^{-9} cm^2/s at 1600 °C. The interdiffusion coefficients for T_2 (~ 10^{-12} cm^2/s) are smaller than that for Mo_5Si_3, although activation energy for interdiffusion of T_2 is nearly comparable to that of Mo_5Si_3. It seems that the 10^4 differences between the interdiffusion coefficients of T_2 and Mo_5Si_3 originates from a difference in prefactor of the interdiffusion coefficient, which is controlled by the atomic jump frequency to adjacent sites. Mo_5Si_3 is generally configured by two Mo and Si sublattice sites, where an atom occupying the Mo sublattice site in Mo_5Si_3 is surrounded by Mo and/or Si species atoms, and an atom on the Si sublattice site surrounded by Mo and/or Si species atoms. However, T_2 is configured by four different sublattice sites. Whenever an atom substitutionally jumps to an adjacent site, it is surrounded by one of four different configurations of Mo, Si, and B atoms and vacancies. It appears that the restricted jump possibilities in T_2, lead to interdiffusion in T_2 that is slower than in Mo_5Si_3; however, a further examination is necessary to resolve this issue.

2.4. Alloying Strategy in Refractory Metal Silicides and Borosilicides

A common feature of the refractory metals is the high mutual solid solution solubility. This trend exists not only in the BCC solutions, but also extends to many intermediate phases (e.g. silicides, borides and aluminides). At

the same time, the sensitivity of the phase stability of silicides in general and T_2 phase in particular to atomic size and off-stoichiometric site substitution suggests that refractory metal substitution for Mo can be an effective approach to controlling phase reactions and a basis to formulate an effective alloying strategy. Previous studies on the alloying behavior of the silicide phases suggested that the incorporation of selected transition metals (W, Nb, V and Cr) results in the formation of a continuous T_2 phase and the two-phase field of BCC + T_2 in the respective quaternary systems (Figure 13)[01Per]. The observed alloying trends also appear to highlight a number of fundamental geometrical factors that influence the relative stability of the T_2 phase and provide a basis to develop modified multi-phase designs[01Per; 03Dim]. There is however limited evaluation on the possible alloying extension of potentially critical additional transition metal (TM) elements for molybdenum alloys such as Group IVB (such as Ti, Zr and Hf) and Group VIIB metals (such as Re). Titanium and hafnium are the major additives to commercial Mo-based alloys such as "TZM" which is composed of a BCC phase and dispersoids of transition metal carbides to enhance the high temperature strength. However, there is no known ternary-based T_2 phase reported in TM-Si-B systems (TM=Ti, Zr and Hf) as shown in Figure 14 [60Par;89Mae;95Vil]. The addition of Rhenium (Re) into a Mo BCC solid solution has been well known to markedly lower the Ductile Brittle Transition Temperature (DBTT) of the BCC phase resulting in a higher ductility and toughness [77Kno].

In general, the size factor metrics such as the atomic radius of the metal components or the atomic radius ratio between metal to metalloids have been shown to play an essential role in alloying extension as exampled by the Hume-Rottery 15 % rule. Similarly, the effect of chemical bonding within the structure as expressed by parameters such as valence electron concentration per atom (e/a) has been shown to be essential in combination with the size factors to define the phase stability. In particular, it has been shown previously that the e/a criteria can be successfully applied to transition metals and transition metal-based compounds [83Ohn;85Fu;87Xu;89Xu;90Xu]. Moreover, the e/a criteria can also be correlated directly to some of the characteristics in the electronic structure of the compounds that favor a high cohesive energy [89Boe]. For example, for a stable and high melting transition metal based BCC phase, the favorable e/a values range between 5.0 (corresponding to that of Group VB metals such as Nb) and 6.0 (corresponding to that of Group VIB metals such as Mo) with the highest cohesive energy (at the ground state) corresponding to an e/a of 5.5 [77Pet;83Wil;89Har]. The optimum e/a value and consequently the maximum cohesive energy are characterized by the electronic structure of the BCC phase showing that all of the bonding states have been filled and none of the anti-bonding states which are at higher energy level are occupied. Furthermore, the extent of solid solution among the transition metals can also be estimated from a similar analysis [77Pet;83Wil;89Har].

While there have been numerous studies of the alloying behavior in BCC refractory metals, the analysis of the alloying behavior in refractory metal silicide phases is relatively limited. In multiphase designs an understanding of the relative solubility of a given addition in each of the coexisting phases is essential to judge how the solute addition is partitioned between phases and the influence of the solute addition on the phase boundaries and relative phase stability. Since the refractory metal intermetallic phases often display variable and asymmetrical homogeneity ranges about the stoichiometric composition, the analysis of alloying behavior requires an examination of the local atomic environment for the components in order to evaluate the key geometric and electronic interactions that

control the relative stability. In the current work, a similar approach to phase stability analysis in terms of on the electronic structure and the level of bonding states occupancy was performed by means of a number of available and well-known ab-initio codes [84Ski,04Sav,And]. Based on the calculated electronic structure, the criteria for the optimum e/a and the transition metal alloying trends were estimated and compared with that calculated for the BCC phase. For intermetallic phases an important compliment to phase stability analysis relates to the constitutional defect structure that governs the extent of departure from stoichiometry and the homogeneity range. In addition to the computational analysis of stability, the predicted behavior was evaluated by experimentally determining selected alloying behavior in order to establish guidelines for the stability in the silicide phases for a wide range of potential alloying elements.

In the current study, all alloys were prepared by repetitive arc melting of high-purity refractory metals, Si and B in an atmosphere of high purity and oxygen gettered argon. The alloy compositions were selected from the BCC + T_2 and BCC+T_2+A15 phase field. Group IV- VIIB metals were systematically substituted for the molybdenum content in the alloys. Subsequently, the alloys were annealed up to 1600°C for times up to 100 hours. Back-scattered SEM (BSE) and powder X-ray diffraction were used to identify the phases present in the cast as well as the annealed alloys. The Balls and Sticks program [http://www.softbug.com/toycrate/bs/index.html] was used to display the crystal structures. The analysis on the structural stability of the silicide phases is based on the atomic radius and the valence electron concentration per atom. The energy band calculations are based on the local-density approximation (LDA) to electronic exchange-correlation effects [80Vos]. The calculations were performed using two different LMTO programs for a comparison purpose: (1) a fast but not highly accurate tight-binding LMASA-47 code [http://www.fkf.mpg.de/andersen/;75And;84And;86And]and (2) an accurate full-potential LMART package [96Sov;04Sov]. The LMASA-47 code utilizes a self consistent tight binding linear muffin-tin orbital (TB-LMTO) method in the atomic sphere approximation (ASA) [75And;84And;86And]. The LMART package utilizes Full-Potential LMTO method (i.e. without any atomic shape approximation). The data of internal atomic positions not restricted by the symmetry (I4/mcm) as well as lattice parameters (a and c) of the Mo_5SiB_2 crystal structure were taken from the reported results of crystal refinement work on single phase T_2 powder [01Raw]. Eigenvalues were calculated over 4500 k-points that represent the reciprocal lattice vectors from the irreducible part of the Brillouin zone. The criteria for the self-consistency were based on the total energy difference from the last iteration to the previous not to exceed 10^{-6} Ry (2.18×10^{-24} Joule). From the calculated electronic structures, the energy level is determined where the occupancy of bonding states are completely filled (typically signified by the presence of a minimum gap) and the e/a value that corresponds to that energy position. The analysis will provide a qualitative assessment on the solubility behavior in the T_2 phase but not necessarily the quantitative phase relations with surrounding phases. Nevertheless, the alloying guidance from this type of an assessment has been proven to be very effective for a wide range of refractory metal based alloys and compounds [89Xu].

2.4.1.Alloying behavior

All of the refractory metal additions from the Group IV, V and VIB metals that were examined show a large degree of substitutional alloying in the T_2 phase and a more limited alloying extent in other silicide structures. As has been shown previously [01Per], in the case of V, Nb ,Cr and W substitutions, there is a continuous solid solution in the T_2 phase based on the samples that were annealed at 1600°C. In the case of Group IVB metal additions, Ti and Hf do not form a complete solid solution in the T_2 phase, however in each case, an extended solubility was observed such that Ti-rich and Hf-rich T_2 phases can be stabilized (i.e. replacement of Mo content exceeds 50 at. %) as shown in Figure 15 and 16. After a substitution of Mo by more than 70 at. %Hf %, the binary HfB_2 phase starts to form during solidification (Figure 16). This implies that the stability of T_2 phase in the quaternary Mo-Hf-Si-B extends deeply into the Hf-rich side. In all cases, the total concentration of the metal components remains close to the stoichiometric value (62.5 at. %), indicating that the refractory metal substitutions strictly replace the Mo atoms at the metal sites in the crystal structure.

The extended alloying solubility in the T_2 phase that mimics the alloying behavior in the BCC phase is not necessarily typical of other Mo-rich boride or silicide phases. For example, the Mo_3Si A15 phase has a very little solubility for W or Nb [00Ma]. The T_1 phase has an extended solubility with Group VB metals, but a more limited one with the Group IVB metals. This is primarily due to the fact that metals such as Hf and Zr tend to stabilize hexagonal based silicides such as the $D8_8$ phase. Similarly, while there is a continuous solid solution with Nb for the Mo_2B phase, there is a little solubility of Ti or Hf in Mo_2B [80Zak].

In contrast to the extended alloying solubility of the Group IV, V and VIB metals, elements in Group VIIB and VIII show a very limited substitution alloying in the T_2 phase. For example, addition of rhenium appears to be very limited in the T_2 phase in two BCC+T_2 alloys that were examined as shown in Figure 17. The rhenium is highly partitioned to the BCC phase (Mo,Re) solid solution instead of the T_2 phase as shown in the EDS spectra.

The limited solubility of nickel to substitute for Mo may be explained from the size effect (the difference in atomic radius is more than 10 %). However, the low solubility of rhenium in the T_2 phase as shown in Figure 17 cannot be simply argued from the geometrical point of view. The atomic radius of rhenium differs from that of molybdenum by no more than 2 %. In order to understand the fundamental basis of the observed alloying behavior it is useful to examine more closely the structural arrangements in the intermetallic phases to elucidate the local environment of the refractory metal that will also impact the governing binding arrangements.

2.4.2. Silicide Phase Structures

For a further examination on the stability of the silicide and borosilicide phase stability, it is useful to examine the crystal structures at the stoichiometric composition. The approach to phase stability analysis in metal-metalloid intermetallics in general has been based on the stacking of atomic layers within the crystal structure [31Hag;60Pau]. The Mo_5SiB_2 (T_2) crystal has a $D8_l$ structure that forms a body-centered tetragonal unit cell (space group I4/mcm). A 3-dimensional drawing of the T_2 (Mo_5SiB_2) structure is shown in Figure 18. The unit cell contains 32 atoms (20 Mo, 4 Si and 8 B atoms) that are situated in layered arrangements along the c axis. From the previous work [57Now;57Now;58Aro;59Aro;60Now], three types of layers have been identified: layer A with only Mo

atoms, layer B with only Si atoms and layer C with a mixture of Mo and B atoms. The structural arrangement of these layers in T_2 has been viewed as the means to achieve an efficient atomic packing between metal atoms such as Mo and metalloid constituents (Si and B in this case) [57Now;57Now2;58Aro;59Aro;60Now]. Based on the radius ratio of the metal atom and the metalloid atoms, variations in the successive stacking based on the A layered arrangement can be constructed [31Hag]. The relatively large difference in atomic radius of the two types of metalloids necessitates stacking arrangements of the A layers that would facilitate two distinct sites. Layer arrangements of A - $A_{1/21/2}$ - $A_{1/21/2}$ - A – A- in the [001] direction are therefore developed in the T_2 structure. The $A_{1/2/1/2}$ layer refers to the A layer that has been translated by half the base diagonal relative to neighboring layers. With the A-$A_{1/21/2}$ or vice versa, a cubic anti-prismatic site is created and filled by Si atoms forming the layer C (see Figure 18). The B atoms on the other hand are situated in the trigonal prismatic hole generated by sandwiching two symmetrically oriented A layers (the A-A or $A_{1/21/2}$ – $A_{1/2/1/2}$ layer arrangements). In this arrangement, the B atoms are capped by two triangular arrangements of Mo atoms along the c axis and one B and two more Mo atoms forming an intermediate layer (layer C). The two Mo atoms fill the remaining available hole created by the A-A layer arrangements that accordingly constitutes the largest hole available (the cubic prismatic hole). Thus, the limited ability to stabilize the T_2 phase in the Si-rich region for the Mo-Si-B system may be interpreted as the difficulty in situating Si atoms in the B sub-lattice in the trigonal prismatic hole site. On the other hand, there is a ready accommodation of B atoms in the Si lattice position which is also indicated by the reduction of the cell volume. The limitation in the enriching the T_2 phase with Si may be related to the limited available volume of the B sub-lattice. Moreover, this behavior is directly correlated with the available cell volume within the T_2 phase homogeneity range and consistent with the observed asymmetric homogeneity range about the stoichiometric composition.

The A layer arrangement in the T_2 phase is not necessarily unique since it is also observed in both borides (Mo_2B) and other silicides (T_1). In fact, the stacking arrangement of such type of layers are part of the larger crystal family of $CuAl_2$-type phases where the radius ratio of the metal to metalloids determine (from the geometric point of view) the types of stacking within the crystal structure. The T_2 phase has the atomic radius ratio 'in-between' the known silicides and borides with comparable amount of metal content (i.e. Mo_2B and Mo_5Si_3). The Mo_2B has a higher radius ratio of metal to metalloid than the Mo_5SiB_2 and it has only one type of metalloid site. Previous studies suggested that due to this relatively a high radius ratio, the boride phase forms a repeated A – $A_{1/21/2}$ atomic stacking (instead of A – $A_{1/21/2}$ - $A_{1/21/2}$ – A stacking sequence in T_2 phase). With the repeated A – $A_{1/21/2}$ layer stacking, only one type of interstitial site (anti-prismatic hole) can be created (similar to the "Si site" in Mo_5SiB_2).

The Mo_5Si_3 (T_1 phase) on the other hand has a radius ratio of metal to metalloid below that of T_2 phase. The normal A – $A_{1/21/2}$ atomic stacking to fill in Si atoms is accommodated by replacing part of the Mo "A" layers with vacancies and Si atoms to form a modified A layer. Hence, in the T_1 phase, there are two types of the Si atoms, one that is sandwiched between the modified A and $A_{1/21/2}$ layers and the one that is within the modified A layers (see Figure 19-20). In both Mo_2B and T_1 phases, there is no stabilization of the A-A layered arrangement.

In this context, it is worthwhile to note the other crystal variants of the T_2 crystal structure, namely the $D8_8$ phase (Figure 21). Similar to the Mo_2B and T_1 phases, the $D8_8$ phase also has alternating atomic layer stacking of 'modified' A layer and $A_{1/21/2}$ layer. The difference is that the modified A layer forms a hexagonal base symmetry

instead of a tetragonal one (like in Mo_2B, T_1 and T_2 phases). In addition, only half of the interstitial sites available from this type of configuration is filled by the metal constituent i.e. Ti in Ti_5Si_3. Unlike the T_2 phase, the $D8_8$ phase is most stable when the base metal is the Group IVB such as Ti or Hf.

2.4.3. Geometric Factors

In general, a key underlying principle of the metalloid solubility in refractory metal silicides highlights the important role of atomic size factor on the structural stability. There is typically a strict range of atomic size ratio of metal to metalloid that is favorable for the structural stability [60Pau]. The T_2 structure has the highest volume packing density among known TM_5X_3 compounds (TM ≡ Transition Metal, X ≡ Metalloid) [57Now; 57Now2; 58Aro; 59Aro; 60Now]. This suggests that the stability is governed by the drive to achieve a high packing density of the metal and metalloid constituents. A manifestation of the size factor is evident in the restriction of the c/a range of all known T_2 phases as shown in Figure 22. Furthermore, there is a general correlation between the radius ratio of the metal to metalloid atoms and the c/a. A systematic analysis on the change of c/a with a substitution of Mo (0.13 nm) by larger size atoms (such as Ti with atomic radius $r_M = 0.16$ nm) as depicted in Table4 clearly shows the consistent trend of an increase in c/a with a corresponding increase in the atomic radius ratio between the transition metal and the metalloid (r_M/r_X). Such a trend is consistent with the drive to retain a high packing density within the T_2 crystal structure. With an increase in the atomic radius ratio between metal to metalloid, there is a corresponding increase the aspect ratio (c/a) of the tetragonal crystal structure in order to minimize the interstitial volume [01Per].

The geometric rule however does not address the fact that there is an unusually large solubility of the refractory metals in the Mo sites even with elements such as Hf or Ti for which the respective RM-Si-B ternary systems exhibit a stable $D8_8$ phase. In fact, the alloying behavior is apparently quite comparable to the alloying behavior of RM substitutions in the Mo BCC phase. The similarity in the alloying between the metal sites in the T_2 and BCC (A2) phases may be traced to the fact that similar to the BCC crystal structure, the T_2 structure also maintains a relatively high coordination number (CN) of metal–metal atomic contacts to retain a relatively close-packed structure [58Aro; 59Aro]. Furthermore, the T_2 crystal structure (I4/mcm) retains a body-centered symmetry for the refractory metals as exemplified by the similar atomic surroundings of Mo atoms at the (0,0,0) and (½, ½, ½) positions in the lattice. The BCC-like environment is quite evident by examining the surroundings of the Mo atomic sites as depicted in the Figure 23. The figure shows that the CN of Mo-center and Mo-edge contacts in the Mo clusters in the T_2 crystal structure is actually eight which is the same as that of the BCC lattice. In fact, the T_2 structure can be viewed as constructed from vertical chains of the BCC-like corner-sharing Mo clusters connected by the anti-prismatic hole filled by Si (Figure 23). Examination of the inter-atomic distances further supports the resemblance[01Raw]. The Mo-Mo inter-atomic distances associated the nearest neighbors are close to those in the BCC lattice as well. The shortest Mo-Mo interatomic distance yields a value of 0.2737 nm (at room temperature) which is quite similar to that of the Mo-Mo interatomic distance in the BCC lattice (0.272 nm).

The presence of the BCC-like characteristics for the metal component can be traced back to the fact that the "A-A" layered stacking is stabilized only the T_2 phase (in comparison to the other silicides as well as borides). Both

the Mo_2B and Mo_5Si_3 phases stabilize only the A- $A_{1/2/1/2}$ atomic stacking. From the perspective of atomic clusters within the crystal structures, due to the symmetry associated with the A- $A_{1/2/1/2}$ atomic stacking, the crystal structures for both phases are dominated by Mo-Si and Mo-B clusters and the BCC-like environment is absent. While there is Mo-Mo contact within the structures, the Mo-Mo interatomic distance are not similar to that in the BCC phase. Instead, there is a characteristic of a very short interatomic Mo-Mo distance within the crystal structures as depicted in Figure 19 and 20. The interatomic distance of Mo-Mo in the T_1 phase is 0.245 nm and the shortest interatomic Mo-Mo distances in the Mo_2B phase is 0.267 nm compared to 0.2737 nm in Mo. Indeed, the consequence of the BCC-like environment in the T_2 phase can be directly linked to the solubility behavior (in comparison to that of Mo_2B and Mo_5Si_3 phases) and the electronic factors such as the e/a ratio (elaborated in the next session).

2.4.4. Electronic Factor

The capability of Group IVB elements to substitute for Mo in Mo_5SiB_2 is unusually large considering the fact that none of the respective TM-Si-B systems stabilizes the T_2 phase and the atomic size difference between Mo and these metals are quite large. The extended solubility goes beyond the geometrical Hume-Rottery 15 % limit. For example, the atomic size of Hf is about 20 % larger than Mo, but the solubility is more than 50 at. %. On the other hand, Re has a more limited solubility in T_2 phase despite a mere 1-2 % difference in atomic size. Therefore, the electronic factors such as the e/a value and the density of states (DOS) must also be evaluated to elucidate the alloying behavior in the borosilicide phase

There have been limited studies on the relationship between alloying behavior and the electronic structure of metal rich silicides and borosilicides [99Fu; 00Fu]. The most recent work has been concentrated mainly on the effect of alloying on the physical properties such as thermal expansion and elastic moduli. In contrast, there have been several phase stability studies that focused on the rare earth (RE) and alkaline-earth (AE) based T_2 phases such as La_5Si_3 and Ca_5Ge_3 where the phase stability criteria may not be similar to that of the transition-metal based T_2 phase. The RE and AE - based T_2 phases can be distinguished from the transition-metal based T_2 phase by the value of the valence electron per atom (e/a). A plot of occurrences of the known T_2 compounds versus the e/a value is shown in Figure 24. Clearly, there is a distinct grouping for the T_2 phase. The low e/ a range (e/a of 2-3) T_2 phase occurs with the metal constituent as the rare-earth or alkaline earth metals and the high e/a range T_2 phase (e/a of 4-5) occurs with a transition metal as the metal atom constituent. It is noteworthy that Mo_5SiB_2 (e/a value 5.0) is positioned at the high end of the e/a range.

Combined criteria that include geometry and electronic factors to define the stability of the T_2 phase are developed in Figure 25 a and b that presents plots of the valence electron concentration per atom (e/a) versus the lattice unit as well as the atomic radius ratio between the metal (r_M) to metalloid/simple metal (r_X) constituent of the T_2 crystal structure. The two domains of T_2 phase can clearly be discerned. More importantly, there are characteristics defining the two groups of T_2 phase. Namely, the low e/a T_2 phase generally has larger lattice dimensions and also a larger atomic radius ratio in comparison to that for the high e/a T_2 phases. The larger lattice

unit is directly correlated to the fact that the metal constituent of the low e/a T_2 phase is composed of either rare-earth or alkaline earth metals which have a larger atomic radius than that for the transition metals. This further confirms a definite correlation between the volumes of the T_2 unit cell with the size of the metal atoms. The relatively high value of the atomic radius ratio of low e/a T_2 phases has another important geometric characteristic. An evaluation of the packing efficiency of the T_2 phase shows that the low e/a T_2 phase also has a much higher volume density per unit cell than that of low e/a T_2 phases (see Figure 26). Thus, there is general tendency for the low e/a value T_2 phases to achieve a relatively high packing efficiency and consequently high atomic radius ratio. One possible explanation of the differences in the relative packing density of the two domains of T_2 phases may be related to the nature of the bonding within the crystal structure, particularly between the metal constituents. In the progression from the rare-earth type of T_2 phase to the transition metal type of T_2 phase, there is an increasing dominance of stronger transition metal-metal bonding due to occupancy of the d electrons. The increasing dependency of the phase stability in the T_2 phase to the directional metal-metal contact appears to limit the degree of packing efficiency of the transition metal-based T_2 phase as indicated in Figure 26. While the packing efficiency of the transition-metal-based T_2 phase remains above 70 %, the packing efficiency of the rare-earth and alkaline-earth-based T_2 phases is even higher. The e/a criterion can be directly related to the electronic structure of the T_2 phase similar to the case of intermetallics in general [77Pet; 83Wil; 89Har]. An 'optimal' e/a would therefore refer to the value of e/a that favors the complete filling of the bonding states [77Pet]. An optimal e/a would therefore bring the highest occupied states (Fermi energy level) of the crystal structure to the position that separates the bonding and anti-bonding states. A low density of states at the Fermi level is favorable for the phase stability. The stability of the BCC phase is favorable with the e/a ratio values between 5-6 with the optimal e/a of 5.5 corresponding to the maximum cohesive energy [77Pet]. The e/a of 5.5 indeed corresponds to the position of the minimum gap in the Density of States (DOS) of the BCC phase. For the BCC phase, the minimum gap in the total DOS is the characteristic energy level that separates the bonding and anti-bonding states of the covalent bond within the crystal structure. The filling of the bonding states has been shown to increase the structural stability of the phase whereas occupation of the anti-bonding states will cause the opposite effect.

For a full phase stability analysis, the role of the vibrational and configurational entropy must also be taken into account and hence the absence of these factors represents one of the major limitations in the analysis developed from the ab-initio calculations at the ground state. However, as has been shown in a wide variety of transition-metal based intermetallics such as silicides, carbides and aluminides [83Ohn; 85Fu; 87Xu; 89Xu; 90Xu], the most stable and highest melting crystal structures tend to exhibit a minimum gap in their total DOS and that the position of the Fermi energy level (which constitutes the highest occupied energy states at the ground state) is very close to the minimum gap. Following this line of reasoning, an analysis on the position of the minimum gap within the total DOS has been performed for the T_2 phase.

The calculated results of the DOS are plotted in Figure 27 for Mo-BCC, Mo_2B ($CuAl_2$ – prototype), T_2 and $D8_8$ phases using the Full-Potential LMTO (LMART) code. The calculated total DOS for the BCC phase correctly reveals a minimum gap corresponding to an e/a value of 5.5 as has been previously reported [77Pet]. In comparison, the e/a value of 4.5 for the T_2 phase is noticeably lower. Indeed, the main reason is due to the fact that the e/a ratio is

the weighted sum of the e/a of the metal component (high VE) and the metalloid (low VE). However, for the metal portions the e/a of 4.5 value means that the critical concentration of valence electrons per TM atom should be 5.2 is still lower than that of the BCC phase (5.5). It is important to note that the Fermi energy level for Mo_5SiB_2 is not at the minimum gap, but at a higher energy level (i.e. the Fermi level lies on the shoulder of the anti-bonding states) suggesting that the anti-bonding states have been partly occupied in Mo_5SiB_2. Hence, in terms of cohesive energy at the ground state, the Mo_5SiB_2 is not the most stable T_2 phase.

In comparison to the T_2 phase, the DOS for the $D8_8$ phase clearly shows that the optimum e/a for the crystal structure is much lower than that of T_2 phase. The transition metal e/a value is barely above 4, meaning that the most stable $D8_8$ phase will have metal constituents that are composed of mostly Group IVB. Indeed, the highest melting $D8_8$ is based on the Group IVB metals (Ti, Zr and Hf-based $D8_8$) [00Kau] which confirms the role of the e/a on the phase stability.

Based on a simple rigid-band approximation [87Xu], the effect of alloying elements with a higher valence electron (VE) than Mo (such as rhenium) can be approximated by simply adding the integrated area of the unoccupied states in the Density of States in the rigid band sense. Conversely, adding alloying elements with a lower valence electron concentration than Mo (such as titanium and niobium) will subtract a portion of the occupied bonding states. From the Density of States of the Mo_5SiB_2, it is clear that the energy position for the minimum gap is slightly lower than the Fermi level position of Mo_5SiB_2. Again, this is due to the fact that the anti-bonding states are partly occupied. Hence, from the perspective of the rigid band model, it is desirable to alloy Mo_5SiB_2 with transition metals with a lower valence electron concentration (such as Group V and IVB metals) to lower the average e/a of the phase or bring it closer to the minimum gap position. On the other hand, addition of metals with a higher e/a ratio (such as Re) may not be as favorable since this would increase the phase e/a to values further away from the 'optimum' e/a value (4.5). Indeed, the alloying experiments confirm the limited solubility of rhenium in the T_2 phase (Figure 17). To achieve the optimum e/a value of the T_2 phase (4.5), the concentration of valence electrons per transition metal atom in the T_2 phase should be close to *5.2*. This value can be achieved for example by having the 1/5 of metal constituent composed of a Group VIB metal such as Mo (VE of 6) and the remaining 4/5 made up of the Group VB metals such as Nb (VE of 5).

The relatively lower optimum metal e/a value for the T_2 phase than that for the BCC phase becomes the major contributing factor to account for the observed alloying behavior. With a lower optimum metal e/a value, the cohesive stability of the ternary-based T_2 crystal structure is centered on the Group VB metals instead Group VIB metals. This appears to be supported by the fact that the melting point of the Nb-based T_2 phase of $Nb_5(SiB)_3$ is actually higher than Mo_5SiB_2 [04Kat]. Another important consequence is the fact that the extent of solubility of Group IVB (with VE of 4) is generally high in the T_2 phase. This again confirms the e/a criterion.

In comparison to the DOS of Mo_2B phase (Figure 27) the alloying for the Mo_5SiB_2 phase with the Group IVB or Group VB metals is much more extensive since the optimum transition metal e/a value for Mo_2B is higher (5.4 versus 5.2). This means that the alloying level with respect to elements such as Nb or Ti will be more limited for the Mo_2B phase in comparison with the T_2 phase. Indeed, the reported ternary Mo-Nb-B and Mo-Ti-B phase diagrams confirm this alloying behavior.

The reasoning for the lower optimum e/a for the T_2 phase (relative to BCC phase) can also be understood as well from the structural point of view. While the atomic layered arrangement as shown in Figure 28 is a convenient way to depict the crystal structure, the T_2 phase is more appropriately illustrated as composed of a dense network of BCC-like Mo-Mo clusters which are surrounded by the Metal-Boron and Metal-Silicon clusters (see Figure 23). The metal-boron cluster forms the 'double-jointed' prismatic trigonal structure whereas the metal-silicon cluster forms the anti-prismatic four Mo atom square surrounding the Si atom. These types of clusters, as has been shown in the previous studies, are present in other types of silicides, carbides or borides [57Now; 58Aro; 59Aro;60Now]. What is unique about the T_2 phase is the fact that the Mo-Mo interatomic distance and the BCC-like symmetry are retained within the crystal structure. It has been established that the underlying physical principle in the phase stability in TM-Metalloid intermediate phases as proposed by Gelatt et. al [83Gel], is the balance between two competing factors; (1) the strong hybridization between the transition metal d states and the s-p states on the metalloids and (2) the weakening of the bonding between transition metal atoms by the departure of the TM-TM interatomic distance from the 'normal' interatomic distance in the pure transition metal to accommodate the metalloids within the compound. Hence, in the T_2 phase, the Mo-Mo contacts are almost undisturbed by the presence of Mo-Metalloid contacts to yield a high cohesive stability.

Typically, TM-Metalloid contacts lead to the shifting of the dominating covalent bonding in the structural stability from TM-TM directional bonding due to d-band interactions to the p-d directional bonding [89Spe; 90Xu]. Due to the BCC-like symmetry of the Mo-Mo cluster, the transition-metal based T_2 phase has a stable structure and relatively high melting point. It is worth noting that the low e/a T_2 phases are stable due primarily to the metal-metalloid contacts within the two polyhedra which is attributed to the p-d hybridization only [98Pot] to distinguish them from TM-based T_2 phase which take advantage of both the p-d hybridization and TM-TM contacts.

The sensitivity of the phase stability to the optimal e/a values can also be illustrated by examining the criterion for the other boride and silicide phases. The relatively lower e/a for the other phases can also be understood from the types of metal-metalloid contacts within the crystal structures. Indeed, with the short metal-metalloid contacts in the Mo_2B, Mo_5Si_3 as well as $D8_8$ phases, the optimum e/a criterion for each one of these phases is lower than that of BCC phase. While the strength of the chemical bonding in the T_2 phase is derived from a mixture of metal-metal and metal-metalloid contacts, the strength of the chemical bonding within the Mo_2B, Mo_5Si_3 or $D8_8$ phases is derived from their metal-metalloid contacts. As a result, the observed solubility becomes more limited. For example, Ti or Hf solubility in Mo_2B is small due to the strong stability of the Ti or Hf-rich boride phases such as TiB_2 and HfB_2. Similarly, the extent of solubility of Group IVB metals in Mo_5Si_3 is limited by the competing hexagonal based phases such as $D8_8$ phases. This again confirms the unique atomic clustering and e/a criteria of the T_2 phase enable the conditions to optimize both Mo-Mo and Mo-metalloid contacts concurrently.

The occurrence of off-stoichiometry in the T_2 homogeneity range can be partly explained by the combination of size and electronic factors. For example, the Mo_5SiB_2 phase is characterized by the anti-site substitution B to Si defect structure. Since the e/a value of Mo_5SiB_2 is 5 which is above the optimum level, the substitution of Si by B is favorable from this perspective to lower the e/a value of the T_2 phase. In contrast, the anti-site substitution for the Nb-based T_2 phase is Si-rich. The e/a value for the stoichiometric Nb_5SiB_2 phase that is not

observed in the homogeneity range of the Nb-based T_2 phase [60Now] would be 4.375 which is lower than the optimum e/a value. The substitution of B by Si will increase the overall e/a value of the Nb-based T_2 phase. Of course, this simplified analysis does not include the contribution of these defect structures to the entropy and thermodynamic properties. Nevertheless, the occurrence of the defect structures appears to be consistent with the e/a based analysis.

To some extent the demarcation of phase stability associated with the metal-metal contact and metal-metalloid contacts is reflected by the two e/a groups of T_2 phase. The low e/a T_2 phases are dominated by the rare-earth metal based compounds whereas the high e/a T_2 phases are based on the transition metals. The chemical bonding associated with the rare-earth metals within the BCC-like cluster relies on the p-d hybridized metal-metalloid contacts within the structure[98Pot]. Hence, even though the crystal structures of the two T_2 compounds are the same, the stabilizing chemical bonding is not the same as depicted in the Figure 17. For the low e/a T_2 phases, the 'skeleton' of the structure is only made of the metal-metalloid contacts whereas the higher e/a T_2 phase is made of *both* metal-metalloid and a network of BCC-like metal-metal contacts.

It is worth noting however that even though the rare earth metals have lower valence electron concentrations than TM there is very little evidence to suggest that there is a large solubility of RE in Mo_5SiB_2 even though the substitution of RE with TM will presumably lower the overall e/a value. Similarly, there is very small solubility of TM in RE-based T_2 phase even though the addition of TM will favor increased phase stability through the metal-metal contacts. In part, this may be explained by the fact that while there may be a favorable electronic factor, the large difference in atomic radius sizes of typical transition metals (0.13 – 0.14 nm) compared to rare-earth metals (0.18 nm) limit the alloying extension. Therefore, both favorable geometrical (atomic size) and e/a criteria must be satisfied to achieve an extended solid solution.

2.2.5 Development in Mo-Ti-Si-B High Temperature Alloys

A combined criteria of e/a and atomic size factor for the transition metals established in the current study can be applied to design multiphase microstructures based on the extended two-phase field of BCC and T_2. The current work enables an alloying strategy needed to further advance the development of Mo-Si-B alloys in general and in particular to yield new high-temperature Mo-Si-B based alloys .One of the main results has been the development of the TZM-like C-doped Mo-Ti-Si-B alloys. The substitution of molybdenum with elements such as titanium is an attractive option the Mo-Si-B alloys since it significantly reduces the weight density. As shown in Figure 29, for a Mo-20Si-10B alloy which is comprised of a two-phase Mo_3Si + T_2, substitution of Mo with Ti will enable the weight density to drop *from slightly above 9 g/cm3 to below 7 g/cm3* (after about 50 % substitution). Nb or Zr substitution can also achieve a similar type of density reduction. Moreover, due to potential substantial solid solution hardening associated with these elements in T_2 phase, a significant enhancement in the high-temperature strength can be expected to ultimately yield lighter and stronger high-temperature materials. It is important to note that despite the significant alloying, the thermal stability of these alloys remains excellent [01PER]. Furthermore, the oxidation resistance of the Mo-Si-B alloys is not compromised by these additions as shown in the recent alloying study in Mo-Ti-Si-B alloys [05SAK].

3. Summary of Research Highlights

Refractory metal silicide phases are often considered to exhibit a relatively high stability as reflected in a high melting temperature. In fact, the high melting temperature and the potential for environmental stability from the development of an SiO_2 surface layer have attracted an increasing attention recently. In particular, alloys in the Mo-Si-B system where the Mo_5SiB_2, T_2, phase is a key constituent have demonstrated the structural and environmental performance that can satisfy the materials challenges of high temperature operation.

In the current investigations several experimental studies of the high temperature stability of the T_2 phase, the diffusion kinetics associated with T_2 phase formation and growth and the influence of selected alloying additions have been pursued together with a modeling analysis of the structural stability. Along with these studies, the characteristic defect structure in the T_2 phase has been identified and new microstructure designs have been developed based upon the guidance derived from the established alloying behavior. For example, the solubility change in the T_2 phase has been measured up to 1950°C and related directly to the development of constitutional vacancies and anti-site defects. An important consequence of the constitutional vacancies is their aggregation and collapse into dislocation loops upon annealing. Moreover, the dislocations act as nucleation sites for Mo precipitation in the T_2 phase. Further, the dislocation character that develops in the T_2 phase appears to depend on the composition and in some cases a faulting is observed that could impact the structural stability. At the same time, the solubility changes with temperature and the defect structure identification in the T_2 phase provide a critical database for the formulation of a computational thermodynamic model for the T_2 phase. Similarly, an essential database for the diffusion kinetics in the T_2 phase is being developed that will be relevant to the analysis and interpretation of high temperature mechanical properties and to the understanding of microstructure changes during oxidation and coating reactions.

A systematic examination of the refractory metal rich silicide phases as well as boride phases reveals some common structural features. In this class, a variety of structure types can be constructed from the different ways of arranging a characteristic layer pattern. The characteristic patterns have been shown to develop over certain well-defined ranges of atom sizes. Several of the arrangements yield a relatively dense packing that serves to maximize the metal-metal contacts within the structure. Within this group, the most efficient arrangement is developed in the T_2 phase. Along with the geometrical requirement that can be identified from the structural analysis, the observed alloying behavior in the silicide phases reveals that the electronic structure also plays a role and is, in some cases, an overriding factor in determining the relative phase stability. The influence of electronic structure factors can be represented in terms of the valence electron concentration per atom. Along with the specific geometric ranges that are associated with the different structures, there is also an electron concentration range that has been identified for given structures. In order to understand the observed alloying behavior within the silicides and borides it is necessary to include both the favorable geometric ranges and the allowed e/a ranges in the analysis. A similar set of geometrical and electronic criteria can be applied to the constitutional defect structures that develop from anti-site substitution. Moreover, the basis of the analysis has been tested in several case studies of solubility behavior and in

the application of controlled alloying additions to alter the multicomponent phase stability. In effect the stability analysis provides essential guidance to develop new multiphase combinations and new microstructures.

4. Personnel Supported

John H. Perepezko Principal Investigator
Ridwan Sakidja Research Associate (partial support)
Sungtae Kim Assistant Scientist (partial support)

5. Publication List

During a research program, substantial time intervals often elapse between the completion of a research study, submission of a manuscript and the final appearance of a paper in print. As a result, the following list gives publications in preparation as well as those in print of in press. (The papers noted by an asterisk are invited).

1. "Transition Metal Alloying and Phase Stability in the Mo-Si-B System", R. Sakidja, S. Kim, J. S. Park and J. H. Perepezko, Mater. Res. Soc. Symp. Proc., 753, pp. BB2.3.1-BB2.3.6 (2003).
2. "Mo-Si-B Alloys: Developing a Revolutionary Turbin Engine Material", D. M. Dimiduk and J. H. Perepezko, MRS Bulletin, 28[9], 639 (2003)
3. "Microstructure development in high-temperature Mo-Si-B alloys", R. Sakidja and J.H. Perepezko, Mater. Res. Soc. Symp. Proc., 851, pp.NN.11.11 (2005)
4. "Nucleation of (Mo) precipitates on dislocations during annealing of a Mo-rich Mo_5SiB_2 phase", N. Sekido, R. Sakidja, and J.H. Perepezko, Mater. Res. Soc. Symp. Proc., 842, pp. S.5.35.1 (2005).
5. "Phase Stability in Refractory Metal Silicides", R. Sakidja and J. H. Perepezko, in The Science of Complex Alloy Phases (ed. P. Turchi and T. Massalski), TMS, Warrendale, PA, 2005, pp. 373.
6. "Phase Stability and Alloying Behavior in the Mo-Si-B System", R. Sakidja and J. H. Perepezko, Metallurgical and Materials Transaction A, 36A, 507 (2005).
7. N. Sekido, R. Sakidja and J. H. Perepezko, Symp. Proc. of Solid-Solid Phase Transformations in Inorganic Materials (TMS, Warrendale, PA), 2005.

Presentations

1-5) The publications (1,3-5,7) were published in the proceedings of the respective conferences and involved presentations as well.

6. "Phase Equilibria and Microstructure Development in Mo-TM-Si-B (TM=Ti, Zr and Hf) Alloys", R. Sakidja, J. Werner, S. Kim and J. H. Perepezko, MS&T '03: Materials Science & Technology 2003, Chicago, IL, Nov 9 – 12 (2003).
7. "Alloy Design and Solidification Microstructures for Mo-Si-B Alloys", R. Sakidja, J. Werner, S. Kim, J.H. Perepezko, Beyond Nickel-Base Superalloys Symposium, TMS Annual Meeting, Charlotte, NC, March 2004.

8. "Mo-Si-B Alloys: A Revolutionary Material for Advanced Ultrahigh Temperature Advanced Turbine Systems", J.H. Perepezko, R. Sakidja and D.M. Berczik, American Ceramic Society, Indianapolis, IN, April 2004.
9. "Structural Stability and Alloying Behavior in Mo_5SiB_2 (T_2) Phase", R. Sakidja and J.H. Perepezko, 10th WIEN Workshop, Penn Sate University, July 12-15, 2004

6. Transitions

Throughout the program we main a close contact with D. Berczik of Pratt & Whitney who is leading a major Air Force/Navy sponsored project on high temperature Mo-Si-B alloys. The PI has also maintained a contact with Dr. D. Dimiduk of WPAFB on the progress of the work.

7. Patents

None to report.

8. Honors/Awards

During the period of the project the PI was elected to Fellow of the TMS and a member of the National Academy of Engineering.

9. References

[31Hag] Hagg, G., Zeitschrift für physikalische Chemie. Abteilung B, 1931, 12: 33.

[57Now] Nowotny, H., E. Dimakopoulou, et al., Monatshefte Fuer Chemie, 1957, 88: 180.

[57Now2] Nowotny, H., R. Kieffer, et al., Planseeberichte Fuer Pulvermetallurgie, 1957, 5: 86.

[58Aro] Aronsson, B. , Acta Chemica Scandinavica, 1958, 12: 31.

[59Aro] Aronsson, B. and G. Lundgren , Acta Chem. Scandinavica, 1959, 13: 433 - 443.

[60Apu] Pauling, L., The Nature of the Chemical Bond, 1960,. Ithaca, NY, Cornell University Press.

[60Now] Nowotny, H., F. Benesovsky, et al. , Monatshefte Fuer Chemie, 1960, 91: 975-990.

[60Par] Parthe, E. and J. T. Norton, Monatshefte Fuer Chemie, 1960, 91: 1127 - 1133.

[64Bar] Bartlett, R.W., P.R. Gage, and P.A. Larssen, Trans. AIME, 1964. 230: p. 1528.

[65Sav] Savitskiy, E.M., et al., Russian Metall., 1965. 2: p. 91.

[71Kuz] Kuz'ma, Y.B., Soviet Powder Metallurgy and Metal Ceramics, 1971. 10: p. 298.

[73Hea] Head, A.K., et al., Computed Electron Micrographs and Defect Identification. 1973, Amsterdam, Netherland: North-Holland

[75And] Andersen, O. K., Physical Review B, 1975, 12: 3060.

[75Klo] Klopp, W., J. Less-Common Met., 42, 261 (1975).

[77Luk] Lukas, H.L., E.T. Henig, and B. Zimmerman, CALPHAD, 1977. 1(3): p. 225-236.

[77Pet] Pettifor, D. G., Journal of Physics, 1977, F 7: 613.

[78Pop] Popula, S. V. , Fomicheva, L., Neorg. Mater. (1978), p. 684-686

[79Kau] Kaufman, L., CALPHAD, 3[1], (1979) p.45

[79Mai] Maier, K., H. Mehrer, and G. Rein, Z. Metallkde., 1979. 90: p. 271

[80Voa] Vosko, S. H., L. Wilk, et al., Can. J. Phys., 1980, 58: 1200.

[81Spe] Spear, K. E., M. S. Wang, CALPHAD, 5[2] (1981), p. 109

[81Sun] Sundman, B. and J. Agren, J. Phys. Chem. Solids, 1981. 42: p. 297.

[83Bir] Birks, N. and G.H. Meier, in Introduction to High Temperature Oxidation of Metals. 1983, E. Arnolds Ltd.: London, UK. p. 54.

[83Gel] Gelatt, C. D., A. R. Williams, et al., Phys. Rev. B, 1983, 27: 2005.

[83Ohn] Ohnishi, S., A. J. Freeman, et al., Phys. Rev. B, 1983, 28: 6741.

[83Wil] Williams, A. R., C. D. Gelatt, et al., Alloy Phase Diagram. L. H. Bennett, T. B. Massalski and B. C. Giessen., 1983, New York, North-Holland: 17.

[84And] Andersen, O. K. and Jepsen O., Physical Review Letters, 1984, 53: 2571.

[84Fra] Franceschi, E.A. and F. Ricaldone, Revue de Chimie Minerale, 1984. 21: p. 202.

[84Kau] Kaufman, L., B. Uhrenius, D. Birnie, K. Taylor, CALPHAD, 8 (1984) , 21.

[84Ole] Olesinski, R. W., G. J. Abbaschian, Bull. Alloy Phase Diagrams 5 (1978) 478.

[84Skr] Skriver, H. L., The LMTO Method, 1984, Berlin, Springer.

[85Atk] Atkinson, K., Elementary Numerical Analysis. 1985, New York, NY: John Wiley & Sons.

[85Fu] Fu, C. L., A. J. Freeman, et al. , Phys. Rev. Lett., 1985, 54(25): 2700.

[86And] Andersen, O. K., Z. Pawlowska, et al., Physical Review B, 1986, 34: 5253.

[87Dir] Dirx, R. R., K. E. Spear, CALPHAD, 11 (1987) 167.

[87Kir] Kirkaldy, J.S. and D.J. Young, Diffusion in the Condensed State. 1987, London, UK: Institute of Metals.

[87Ros] Ross, E.R. and C.T. Sims, in Superalloys II, C.T. Sims, Editor. 1987, John Wiley & Sons, Inc.: New York, NY. p. 97.

[87Sto] Stoloff, N.A., in Superalloys II, C.T. Sims, Editor. 1987, John Wiley & Sons, Inc.: New York, NY. p. 61.

[87Xu] Xu, J.-H., T. Oguchi, et al., Phys. Rev. B, 1987, 35(6940).

[89Boe] Boer, F.R., et al., Cohesion in Metals - Transition Metal Alloys. 1989: Elsevier Science.

[89Har] Harrison, W. A., Electronic Structure and the Properties of Solids. ,1989, New York, Dover.

[89Li] Li, R.-Q., Calphad, 1989. 13(1): p. 61-65.

[89Mae] Maex, K., G. Ghosh, et al., J. of Materials Research, 1989, 4(5): 1209- 1217.

[89Spe] Speier, W., L. Kumar, et al., J. Phys. : Condens. Matter, 1989, 1: 9117 - 9129.

[89Vah] Vahlas, C., P. Y. Chevalier, E. Blanquet, CALPHAD, 13[3] (1989) 273.

[89Xu] Xu, J. and A. J. Freeman, Physical Review B, 1989, 40(11): 11927.

[90Dys] Dyson, B.F. and M.M. Lean, JISI Int., 1990. 30: p. 802.

[90Xu] Xu, J.-H. and A. J. Freeman, Phys. Rev. B, 1990, 41: 12 553.

[91Kim] Kim, Y.W. and D.M. Dimiduk, JOM, 1991. 43: p. 40.

[92Bin] Binder, K. and D.W. Heermann, Monte Carlo Simulation in Statistical Physics. 1992, Berlin: Springer.

[92Boe] Boettinger, W.J., J.H. Perepezko, and P.S. Frankwitcz, Mater. Sci. and Eng., 1992. A155: p. 33.

[92Dim] Dimiduk, D.M., D.B. Miracle, and C.H. Ward, Mater. Sci. and Tech., 1992. 8: p. 367.

[92Kub] Kubaschewski, O., C.B. Alcock, and P.J. Spencer, Materials Thermochemistry. 1992, Oxford, UK: Pergamon Press.

[92Sha] Shah, D.M., et al., Mater. Sci. and Eng., 1992. A155: p. 45.

[92Vas] Vasudevan, A.K. and J.J. Petrovic, Mater. Sci. and Eng., 1992. A155: p. 1.

[93Tho] Thom, A.J., et al., in Processing and Fabrication of Advanced Material for High Temperature Applications III, T.S. Srivitsan and V.A. Ravi, Editors. 1993, TMS: Warrendale, PA. p. 413.

[94Alm] Alman, D.E. and N.S. Stoloff, in High Temperature Silicides and Refractory Alloys, C.L. Briant and e. al., Editors. 1994, MRS: Pittsburgh, PA. p. 255.

[95And] Anderson, I.M., A.J. Duncan, and J. Bentley, Mater. Res. Soc. Symp. Proc., 1995. 364: p. 443.

[95Coh] Cohen, T. H. and M. E. Glicksman, Modelling and Simulation in Materials Science and Engineering, 1995, 3(5): p. 585-96.

[95Gas] Gaskell, D.R., Introduction to the Thermodynamics of Materials. 1995, Washington, DC: Taylor & Francis.

[95Vil] Villars, P., A. Prince, and H. Okamoto, in Handbook of Ternary Alloy Phase Diagrams. 1995, ASM International: Materials Park, Ohio. p. 5520, p. 5704-5705.

[96Sav] Savrasov, S. Y., Phys. Rev. B, 1996, 54: 16470.

[97Nun] Nunes, C.A., R. Sakidja, and J.H. Perepezko, in Structural Intermetallics 1997, M.V. Nathal, et al., Editors. 1997, TMS: Warrendale, PA. p. 831.

[97Per] Perepezko, J.H., et al., in High Temperature Ordered Intermetallic Alloys VII, C.C. Koch, et al., Editors. 1997, MRS: Pittsburgh, PA. p. 1.

[98Pot] Pottgen, R., R.-D. Hoffmann, et al., Z. anorg. allg. Chem., 1998, 624: 945.

[98Sak] Sakidja, R., H. Sieber, and J.H. Perepezko, in Molybdenum and Molybdenum Alloys, A. Crowson, et al., Editors. 1998, TMS: Warrendale, PA. p. 99.

[98Sch] Schneibel, J.H., et al., Scripta Mater., 1998. 38: p. 1169.

[99Day] Dayananda, M.A. and Y.H. Sohn, Metall. Mater. Trans. A, 1999. 30A: p. 535.

[99Fu] Fu, C. L., X. Wang, et al., Intermetallics, 1999, 7: 179 -184.

[99Sak] Sakidja, R., et al., in High Temperature Ordered Intermetallic Alloys VIII, E.P. George, M. Yamaguchi, and M.J. Mills, Editors. 1999, MRS: Pittsburgh, PA. p. KK6.3.1.

[99Sak2] Sakidja, R., H. Sieber, and J.H. Perepezko, Phil. Mag. Lett., 1999. 79: p. 351.

[99Sch] Schneibel, J.H., et al., Mater. Sci. and Eng. A, 1999. 1-2: p. 78.

[And] http://www.fkf.mpg.de/andersen/.

[Sof] http://www.softbug.com/toycrate/bs/index.html.

[00Alf] Alfe, D., et al., Int. J. Quantum Chem., 2000. 77: p. 871.

[00Fou] Fournelle, J.H., et al. . in Proceeding of 2nd Conference of International Union of Microbeam Analysis

Societies (IUMAS). 2000. Kailua-Kona, Hawaii, July 9-13.

[00Fu] Fu, C. L. and X. Wang, Phil. Mag. Letters, 2000, 80(10): 683.

[00Hue] Huebsch, J.J., et al., Intermetallics, 2000. 8: p. 143.

[00Liu] Liu, Y., G. Shao, and P. Tsakiropoulos, Intermetallics, 2000. 8: p. 953.

[00Ma] Ma, C.-L., Y. Tan, et al., Materials Transactions, JIM, 2000, 41: 1329-1336.

[00Nun] Nunes, C.A., et al., Intermetallics, 2000. 8: p. 327.

[00Ros] Rosales, I. and J.H. Schneibel, Intermetallics, 2000. 8: p. 885.

[00Sak] Sakidja, R., et al., The International Journal of Refractory Metals and Hard Materials, 2000. 18(4-5): p. 193.

[01Fie] Field, R.D., et al., International Symposium on Deformation and Microstructures in Intermetallics. 2001, Warrendale, PA: TMS

[01Ful] Fultz, B. and J.H. Howe, in Transmission Electron Microscopy and Diffractometry of Materials. 2001, Springer-Verlag: Berlin, Germany. p. Chpts. 7, 10.

[01Goe] Goeken, M., et al., Materials Science and Engineering A, 2001. 319-321: p. 902-908.

[01Kim] Kim, S., et al., in High Temperature Ordered Intermetallic Alloys IX, J.H. Schneibel, et al., Editors. 2001, MRS: Pittsburg, PA. p. N5.42.1.

[01Per] Perepezko, J. H., R. Sakidja, et al., High Temperature Ordered Intermetallic Alloys IX. J. H. [01SCH] Schneibel, S. [01han] Hanada, K. J. Hemker, R. D. Noebe and G. Sauthoff., 2001, Pittsburgh, PA, MRS: N4.5.1.

[01Raw] Rawn, C.J., et al., Intermetallics, 2001, 9: p. 209.

[01Zai] Zaitsev, A. I., A. A. Kodentsov, J. Phase Equilibria, 22 (2001), 126

[03Dim] Dimiduk, D. M. and J. H. Perepezko, MRS Bulletin, 2003, 28(9): 639.

[04Alu] Alur, A.P., N. Chollacoop, K.S. Kumar, Acta Materialia 52 (2004) 5571–5587

[04Kat] Katrycha, S., A. Grytsiva, et al., Journal of Solid State Chemistry, 2004, 177(2): 493-497.

[04Sav] Savrasov, S. Y., http://physics.njit.edu/~savrasov/, 2004

[05Med] Medvedeva, N. I., Y. N. Gornostryrev and A. J. Freeman, Phys. Rev. Lett., 94, 136402 (2005).

[05Sak] Sakidja, R. and J.H. Perepezko, MRS Symp. Proc., Vol. 851 (2005), pp. NN.11.11.1-NN.11.11.6.

[05Sch] Schneibel, J. H., R. O. Ritchie, J. J. Kruzic and P. F. Tortorelli, Met. Trans. A, 36A, 2005; p. 525,

[05Sek] Sekido, N., Sakidja, R. and J.H. Perepezko, MRS Symp. Proc. Vol. 842 (2005), S5.35.

[05Yan] Yang, Y., Chang, Y. A., Intermetallics 2005; 13: 121-128.

[05Yan2] Yang, Y., Chang, Y. A., Tan, L., Cao, W., Acta Materialia 2005; 53: 1711-1720.

10. Tables

Table 1. Si and B solubility ranges of Mo, molybdenum silicides, and molybdenum borides in the Mo-rich Mo-Si-B system at various temperatures, as shown in **figure** 1.

Temp. (°C)		Mo(ss)	Mo_2B	MoB	Mo_3Si	Mo_5Si_3
1600	at%Si	0 – 2.91	0 – 0.09	0 – 0.06*	24.24 – 25.43	≥ 37.3*
	at%B	0	32.97 – 34.03	≥ 48.13*	0	0*
1870	at%Si	0 – 5.40	0 – 0.43	0 – 0.08*	23.75 – 25.25	≥ 37.3*
	at%B	0 – 0.22	31.76 – 33.86	≥ 47.89*	0	0*
1950	at%Si	0 – 6.08	0 – 1.79	0 – 0.09*	25.20**	≥ 37.3*
	at%B	0 – 1.29	31.44 – 33.82	≥ 47.83*	0**	0*

* Due to study on the Mo-MoB-Mo_5Si_3 region, phase boundary compositions on the B rich side of MoB and on the Si rich side of Mo_5Si_3 have not measured.

** Due to melting of a Mo(ss)+T_2+Mo_3Si above 1870 °C, phase boundary composition on the Mo rich side of Mo_3Si could not measured.

Table 2. Change in the lattice parameters of T_2 phase during annealing.

	a (nm)	*c* (nm)	v (nm^3)
As-Cast	0.5982	1.1054	0.3956
1550 °C / 20 h	0.5986	1.1061	0.3964
1550 °C / 100 h	0.6006	1.1065	0.3991

Table 3. Energy factors and elastic line energies for possible dislocations in T_2 phase.

b	***ξ***	Character	K (GPa)	E (nJ/m)
[100]	[001]	Edge	205	73.9
[100]	[010]	Edge	209	75.5
[100]	[100]	Screw	158	57.0
$\frac{1}{2}$[111]	[-110]	Edge	199	96.2
$\frac{1}{2}$[111]	[111]	Screw	145	70.2
[110]	[001]	Edge	205	147.9
[110]	[-110]	Edge	205	147.9
[110]	[-111]	Edge	208	150.6
[110]	[110]	Screw	165	119.4
[001]	[100]	Edge	194	236.3
[001]	[110]	Edge	193	235.0
[001]	[001]	Screw	174	211.7

Table 4 Lattice parameters of the T_2 phase with increasing substitution of Mo by Ti

Nominal Composition	% of Ti substitution	*a* (in nm)	*c* (in nm)	*c/a*
Mo-5Ti-10Si-20B	7 %	0.60040	1.1048	1.8401
Mo-20Ti-10Si-20B	28 %	0.60077	1.1108	1.8490
Mo-31.25Ti-12.5Si-25B	50 %	0.60434	1.1234	1.8589
Mo-40Ti-20Si-10B	57 %	0.60571	1.1267	1.8601
Mo-50Ti-20Si-10B	71 %	0.60650	1.1332	1.8684

7. Figures

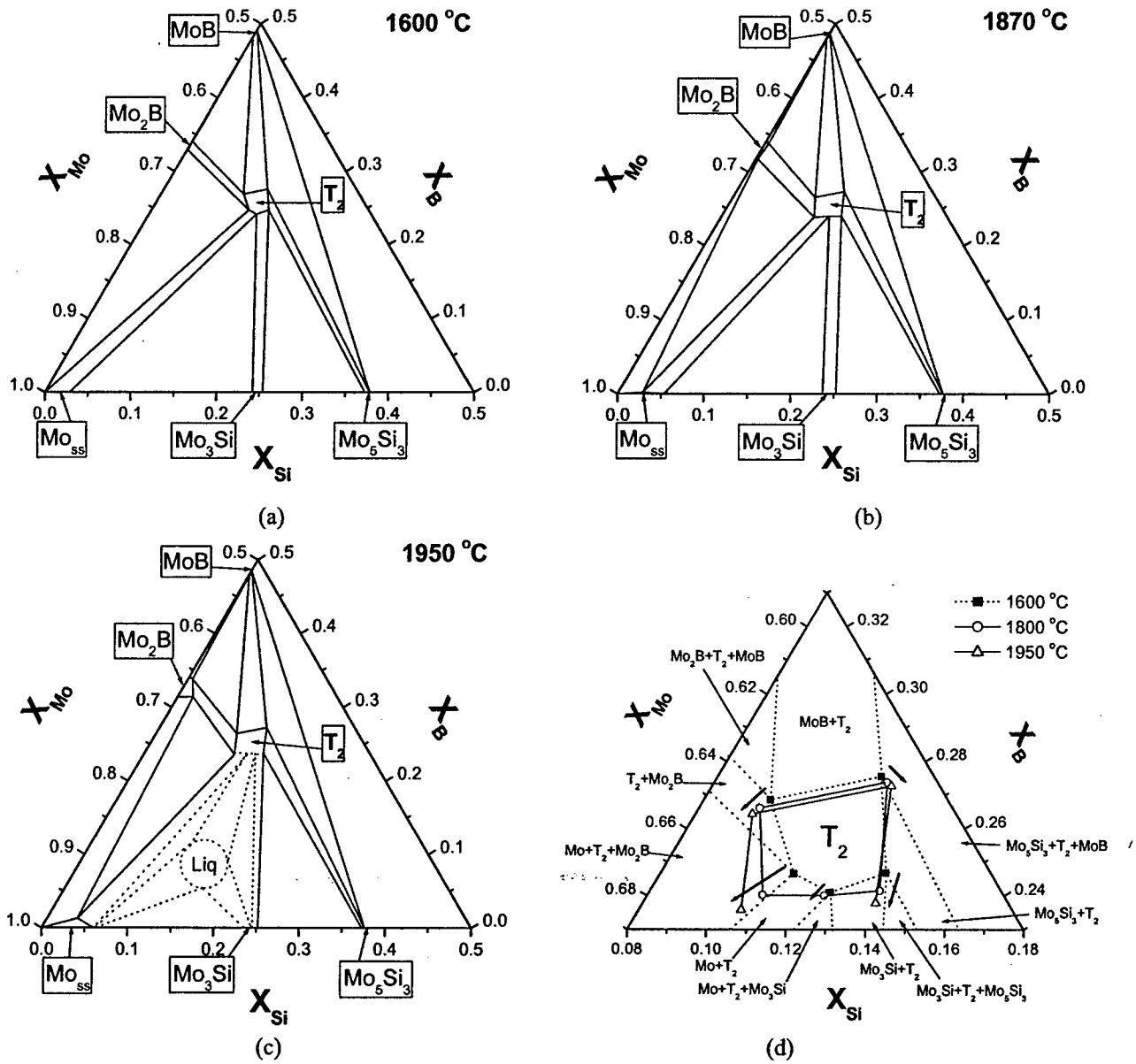

Figure 1. Isothermal sections in the Mo-rich Mo-Si-B system at (a) 1600 °C, (b) 1870 °C and (c) 1950 °C, and (d) summary of the T_2 phase stability changes. The arrows on the edges of the T_2 phase field indicate the direction of solubility change with increasing temperature.

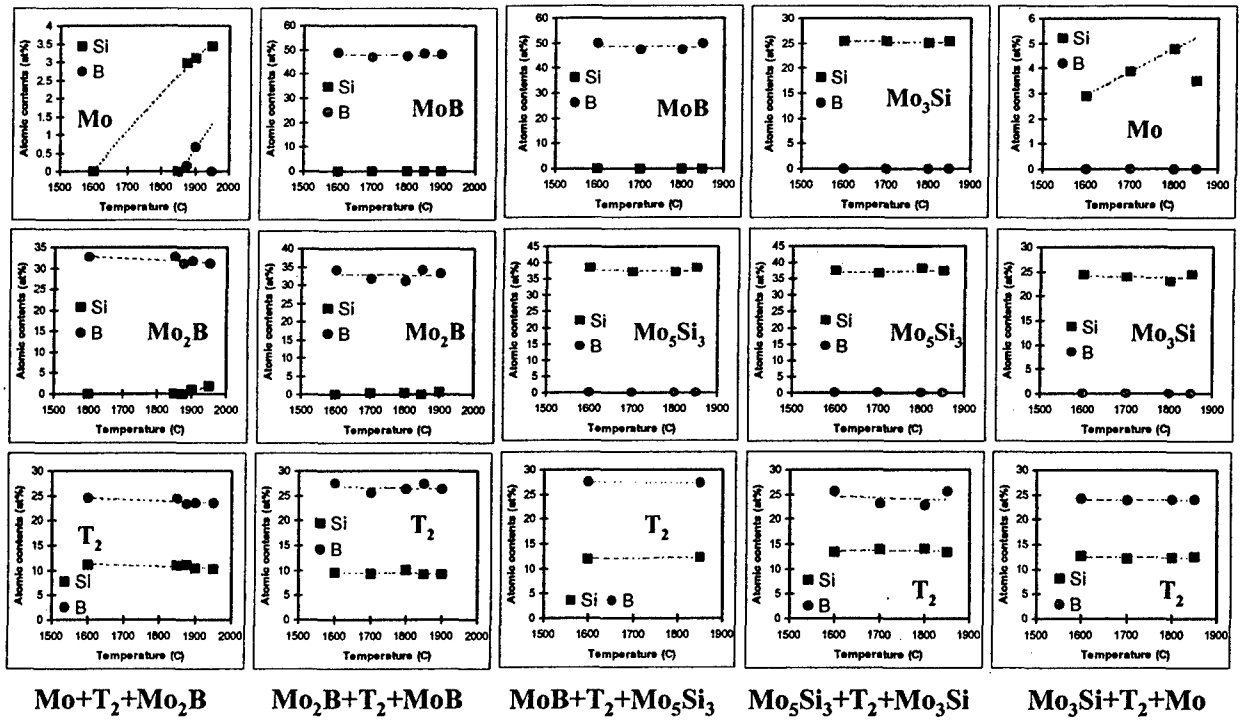

Figure 2. Variation of Si and B solubilities as a function of temperature

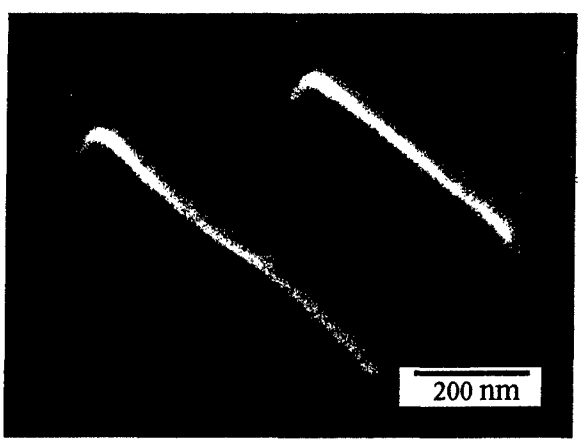

Figure 3 Mo(ss) precipitates in the T_2 phase matrix

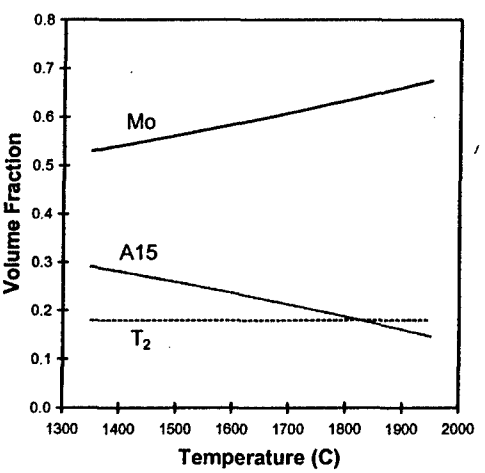

Figure 4. The volume fraction changes of Mo(ss), T_2 and A15(Mo_3Si) in an $Mo_{85}Si_{10}B_5$ alloy.

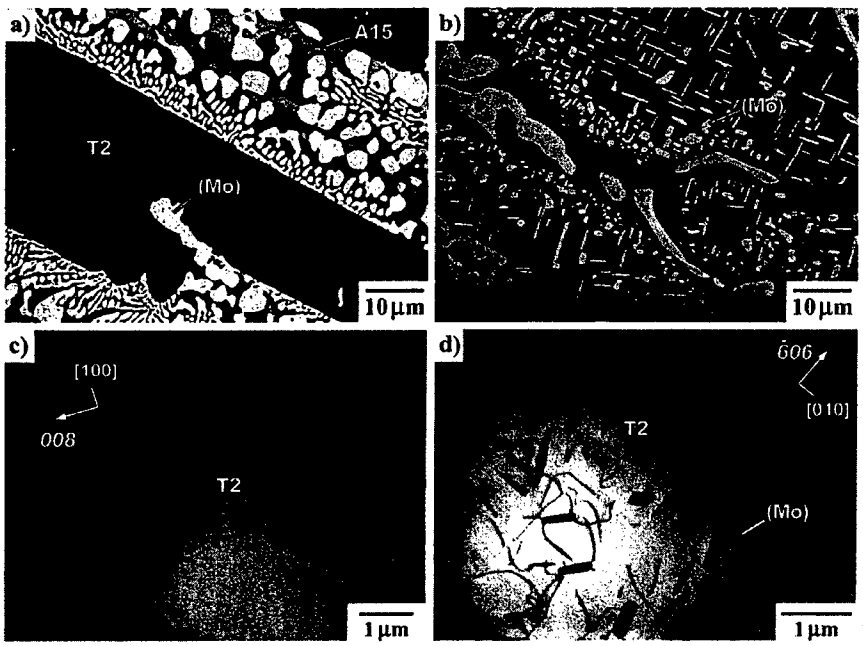

Figure 5 SEM micrographs for Mo-10Si-20B alloys; a) as-cast, b) annealed at 1600 °C for 150 hours, and TEM micrographs for the T_2 phase of Mo-10Si-20B alloys; c) as-cast, d) annealed at 1550 °C for 20 hours.

Figure 6 Weak-beam dark field images of the dislocation in T_2 phase under a) $\boldsymbol{g} = \boldsymbol{-1-23}$, b) $\boldsymbol{g} = \boldsymbol{220}$, *and* c) $\boldsymbol{g} = \boldsymbol{-110}$. The numbers of excess thickness fringes terminated at the ends of the dislocation are consistent with the products of each $\boldsymbol{g}$ and $\boldsymbol{b}$ = [-1,-1,0].

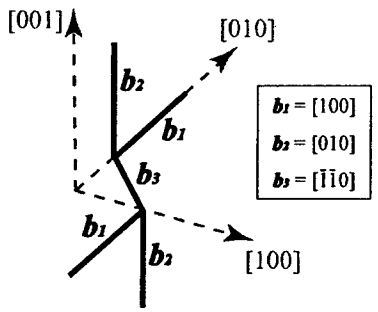

Figure 7 Schematic of a segment of the dislocation network formed in the T_2 phase of Mo-10Si-20B alloy annealed at 1823 K for 20 hours. The dislocation network is mainly composed of edge dislocations with Burgers vectors of <100] and <110].

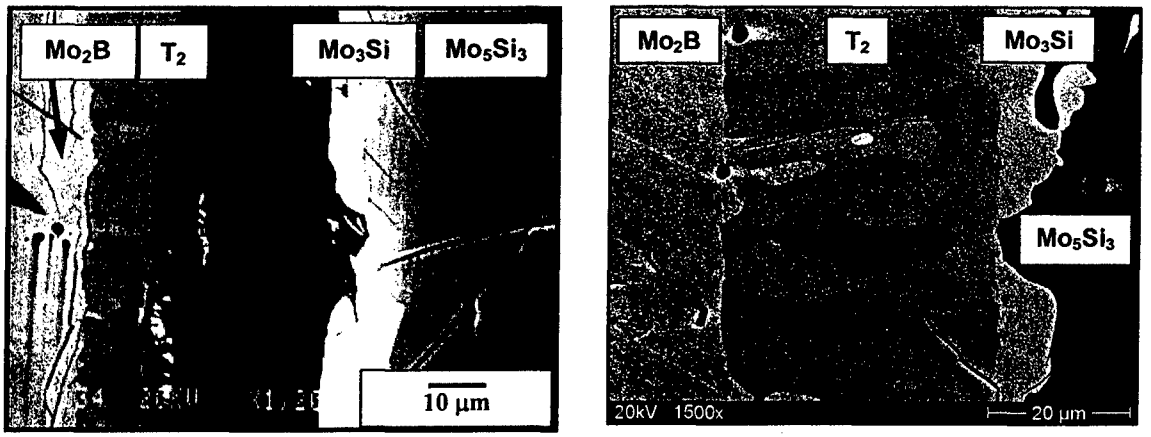

(a) (b)

Figure 8 BSE images of cross-sections of the Mo_2B/Mo_5Si_3 diffusion couples heat-treated at 1600°C for (a) 100 hrs and (b) 805 hrs

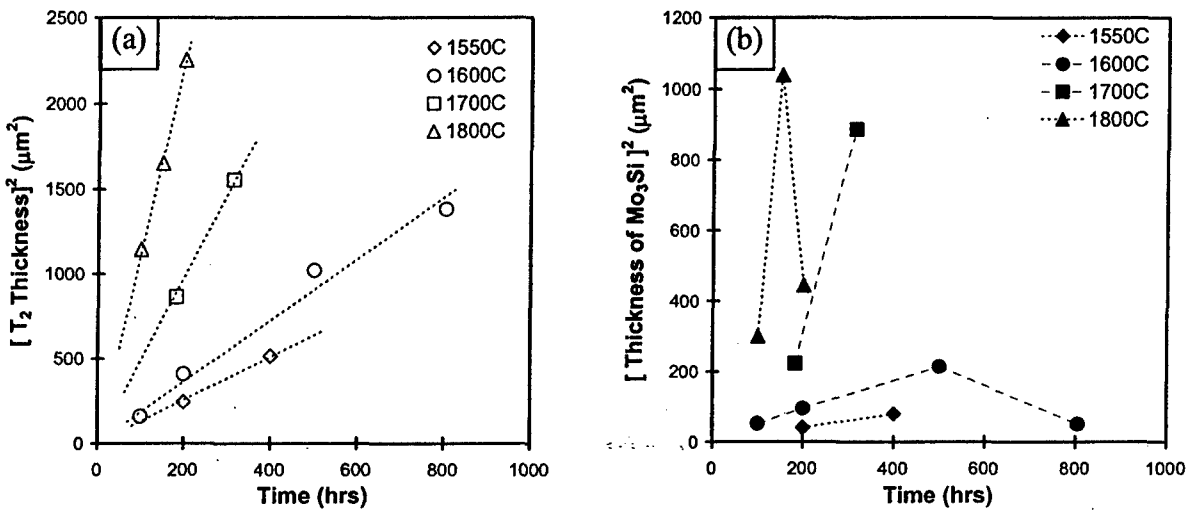

Figure 9. Measured thickness of (a) T_2 and (b) Mo_3Si phases versus annealing time for a Mo_2B/Mo_5Si_3 diffusion couple

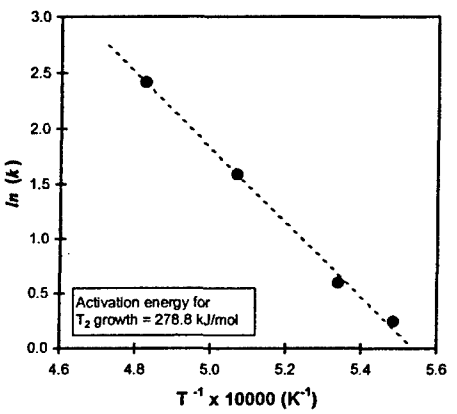

Figure 10. Plot of the rate constant of the T_2 phase versus reciprocal temperature

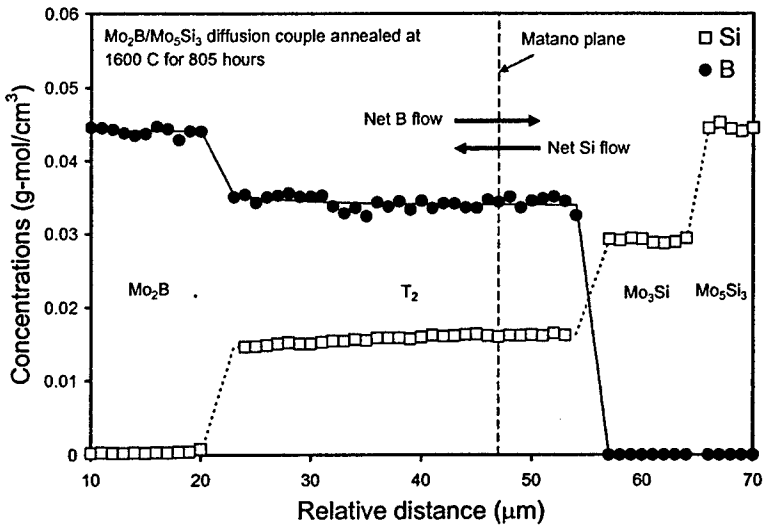

Figure 11. Concentration profiles of Si and B obtained from EPMA measurements on the Mo_2B/Mo_5Si_3 diffusion couple annealed at 1600 °C for 805 hours. Concentrations are expressed as g-mol/cm^3 through the use of molar volumes of all identified phases (7.318 cm^3/g-mol for Mo_2B, 7.696 cm^3/g-mol for T_2, 8.805 cm^3/g-mol for Mo_3Si, and 8.535 cm^3/g-mol for Mo_5Si_3). Solid and dotted smooth lines are drawn by numerically fitting a polynomial equation on concentration profile data.

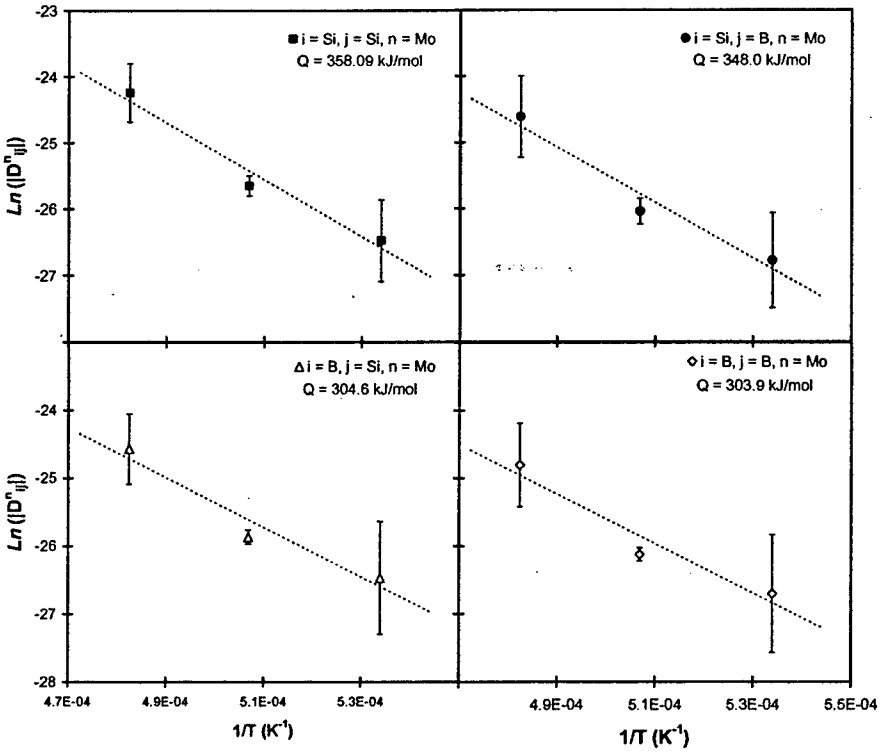

Figure 12. Arrhenius plot of average interdiffusion coefficients versus reciprocal temperature to indicate the activation energy for each $\tilde{D}_{ij}^{n}$, (i, j = Si and B, and n = Mo). Due to negative values of $\tilde{D}_{BSi}^{Mo}$ and $\tilde{D}_{BB}^{Mo}$, their absolute values were used in the plots.

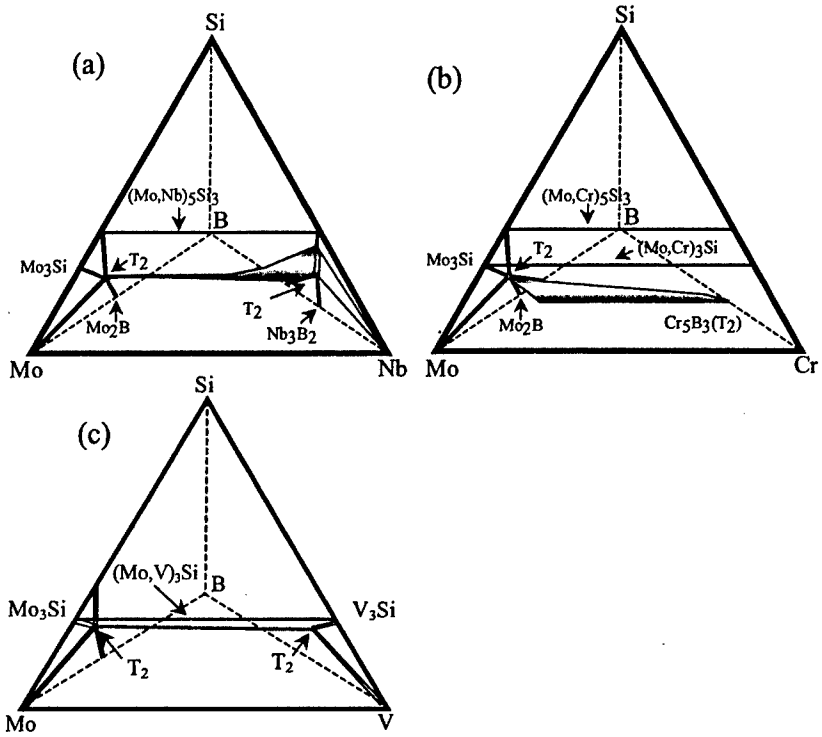

Figure 13. Schematic illustration of observed solubility for selected transition metal additions in both the BCC and the T_2 phase in the Quaternary Mo-TM-Si-B Systems of a) Mo-Nb-Si-B b)Mo-Cr-Si-B and c)Mo-V-Si-B.

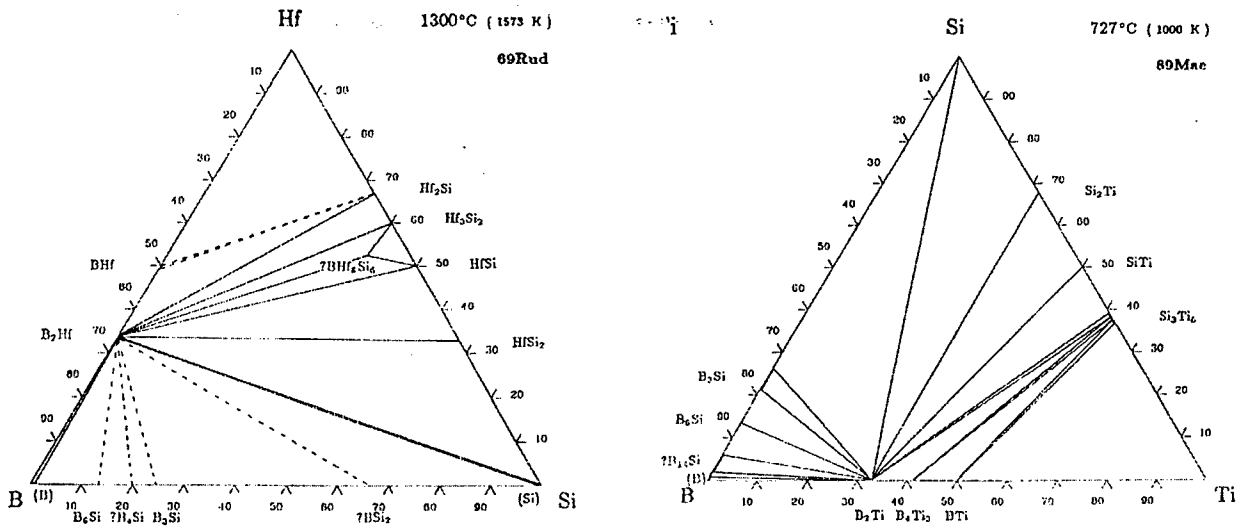

(a) (b)

Figure 14 The reported isotherm in a) Hf-Si-B at 1300°C and b) Ti-Si-B at 727°C showing the absence of the ternary-based T_2 phase [89Mae;60Pat] .

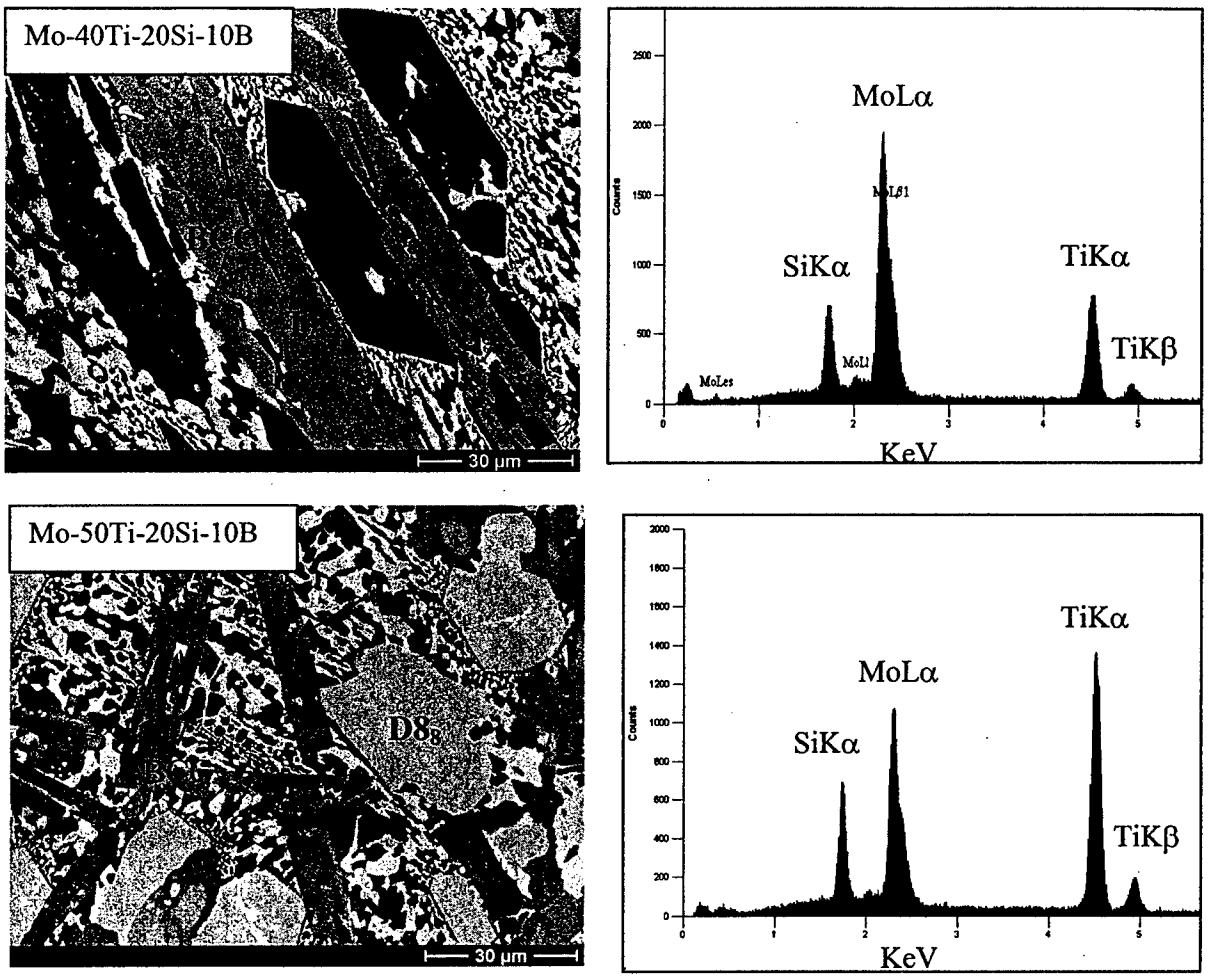

Figure 15 Back Scattered SEM images of Ti-Substituted Mo-Si-B Alloys and EDS Spectrum on Ti-rich T_2 Phase.

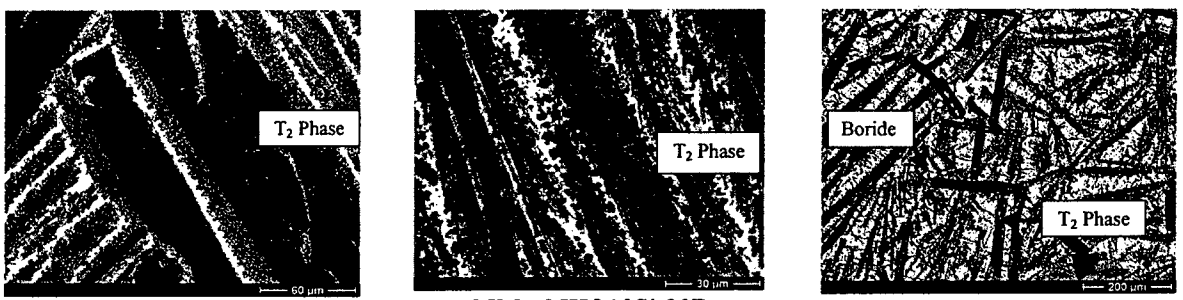

65Mo-5Hf-10Si-20B 35Mo-35Hf-10Si-20B 20Mo-50Hf-10Si-20B

Figure 16 Back Scattered SEM images of Mo-Si-B alloy microstructures that develop at increasing level of Hf substitutuion for Mo.

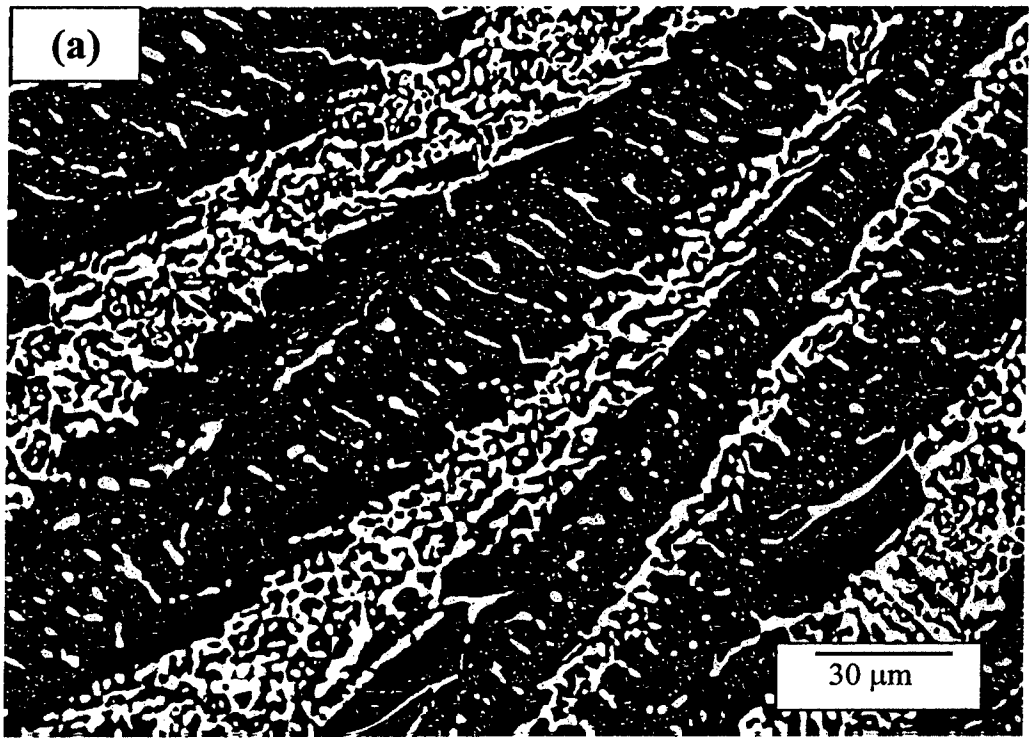

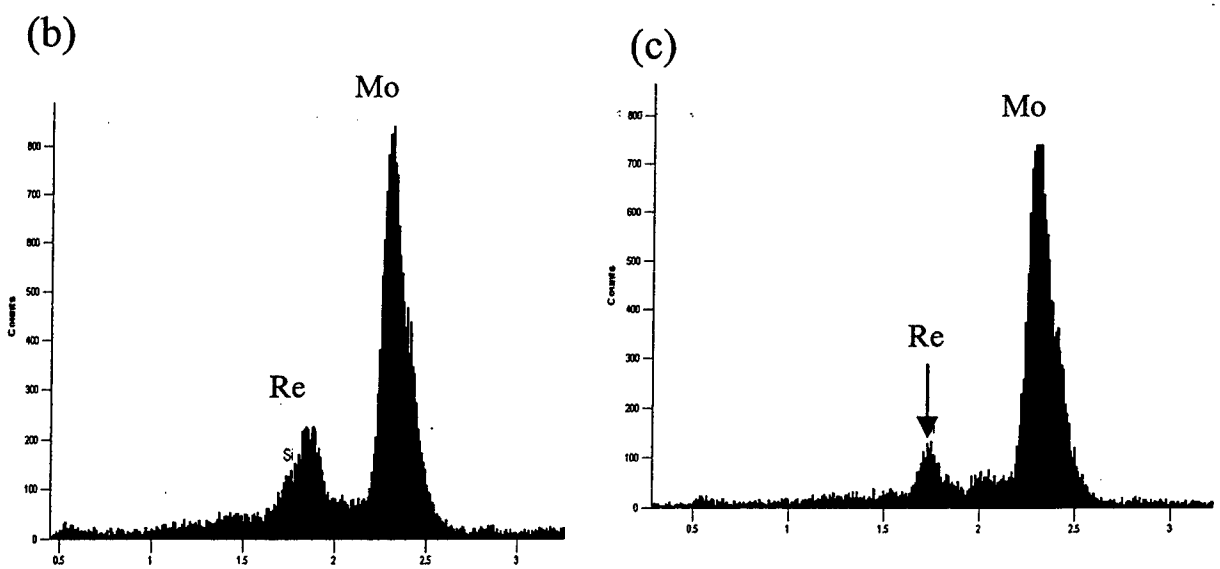

Figure 17: a) BSE image of Mo-5Re-10Si-20B alloy microstructure after annealing at 1600°C (150 h) showing the T_2 (dark) and BCC (bright) phases. The EDS spectra in (b) indicates 8 at. % solubility of Re in the BCC phase. In contrast, the spectra from the T_2 phase (c) indicates the solubility of Re to be less than 1 at. %.

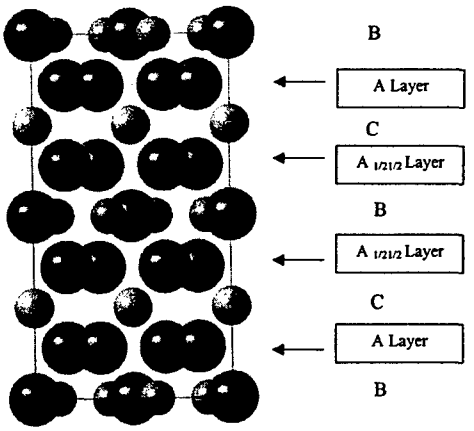

FIGURE 18 T_2 Crystal Structure comprised of stacking of Mo only atomic layer (A layer) , Mo + B atomic layer (B) and Si only atomic layer (C) . The atomic arrangement of the A layer and A ½ ½ layer are illustrated in b and c.

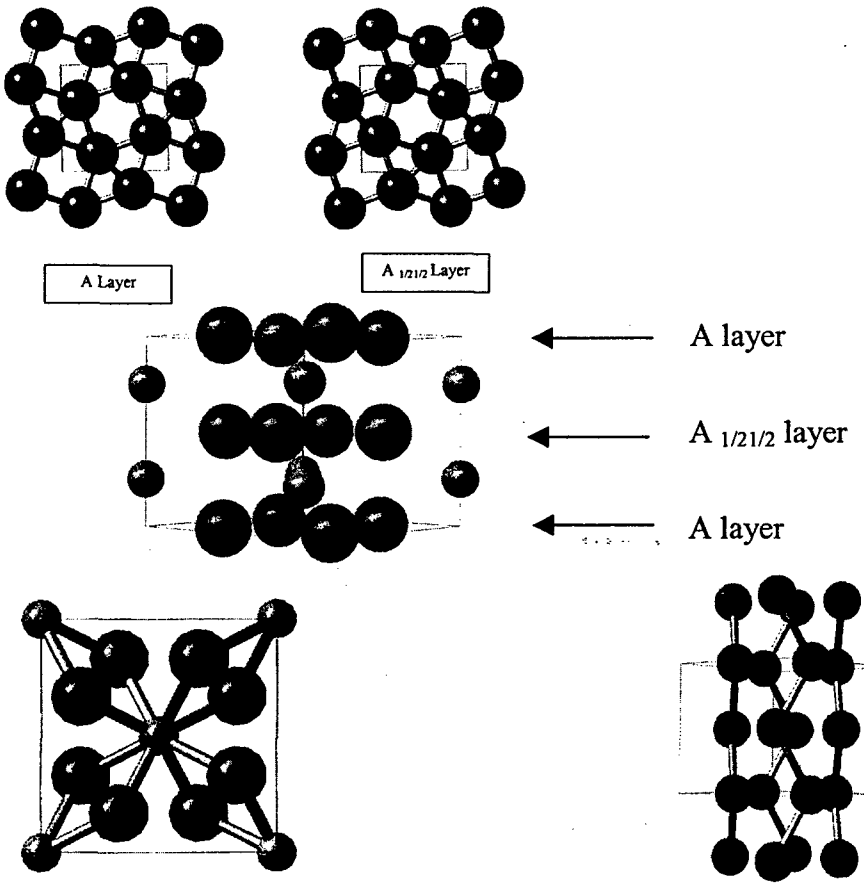

The A- $A_{1/2/1/2}$ layered arrangement yield the Mo-B clusters in Mo_2B

Mo-Mo chains in Mo_2B phase with an interatomic distance of 0.267 nm

FIGURE 19 Crystal Structure of Mo_2B phase showing the alternating sequence of the modified A and $A_{1/21/2}$ layers bordering the B only layers. The crystal structure is also characterized by the presence of Mo-Mo vertical chain similar to that of the T_1 phase (Figure 20).

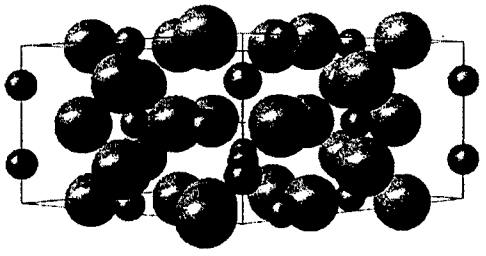

Modified A layer

Modified A $_{1/21/2}$ layer

Modified A

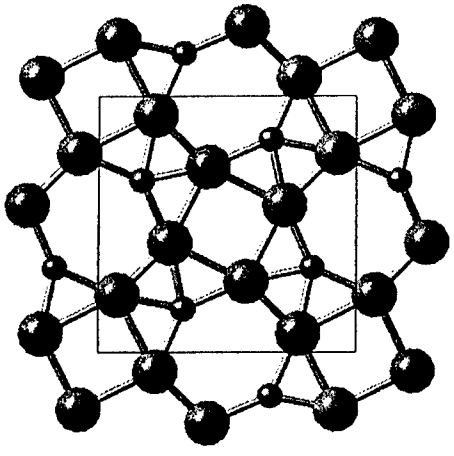

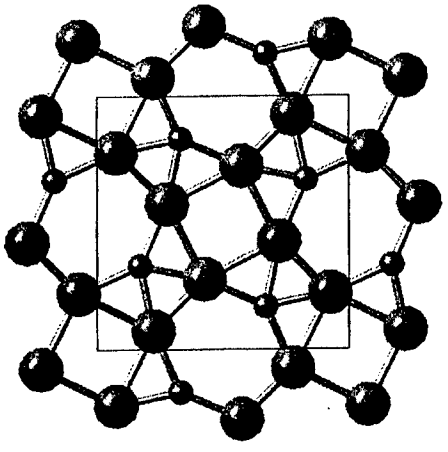

Modified A layer

Modified A $_{1/21/2}$ layer

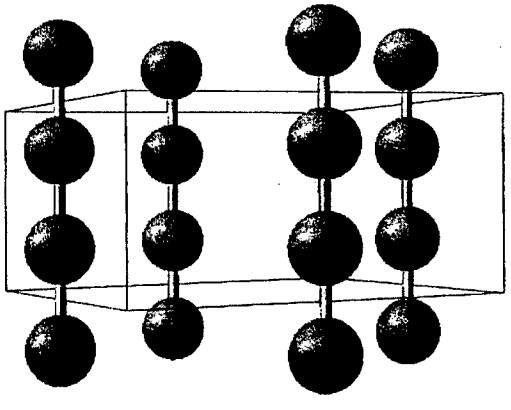

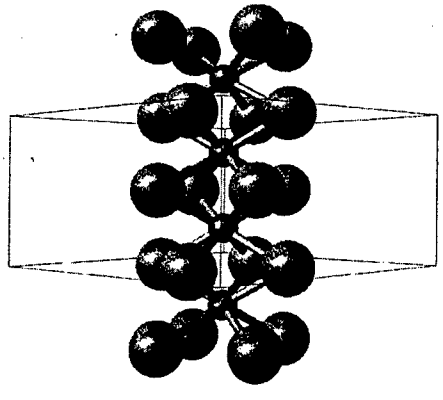

Mo-Mo chains in Mo_5Si_3 phase with an interatomic distance of 0.245 nm

The Mo-Si clusters within the Mo_5Si_3 phase from the A-A $_{1/2/12}$ stacking

FIGURE 20 Crystal Structure of Mo_5Si_3 (T_1) phase phase showing the alternating sequence of modified A and A $_{1/21/2}$ layers. The atomic arrangements of the modified A layer and A $_{½ ½}$ layer are illustrated..

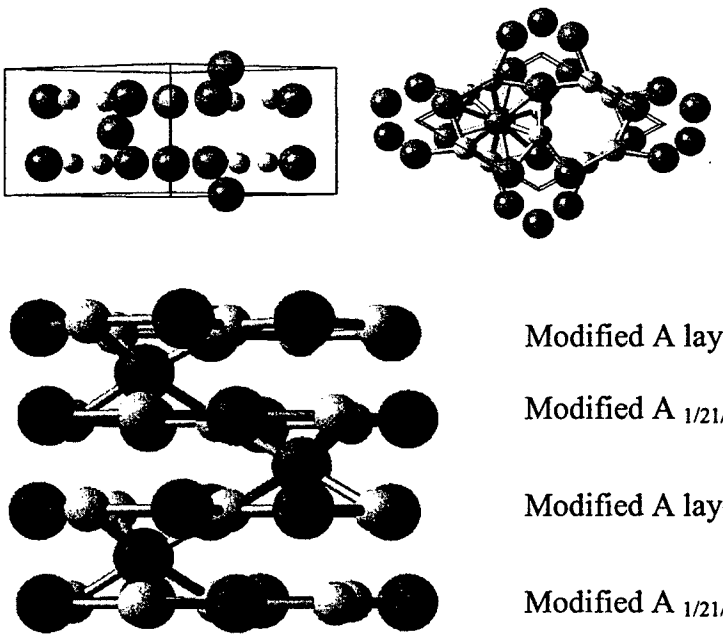

FIGURE 21 Crystal Structure of Ti_5Si_3 ($D8_8$) phase showing the alternating sequence of the modified A and A $_{1/21/2}$ layers bordering the half-filled Mo-only B' layer.

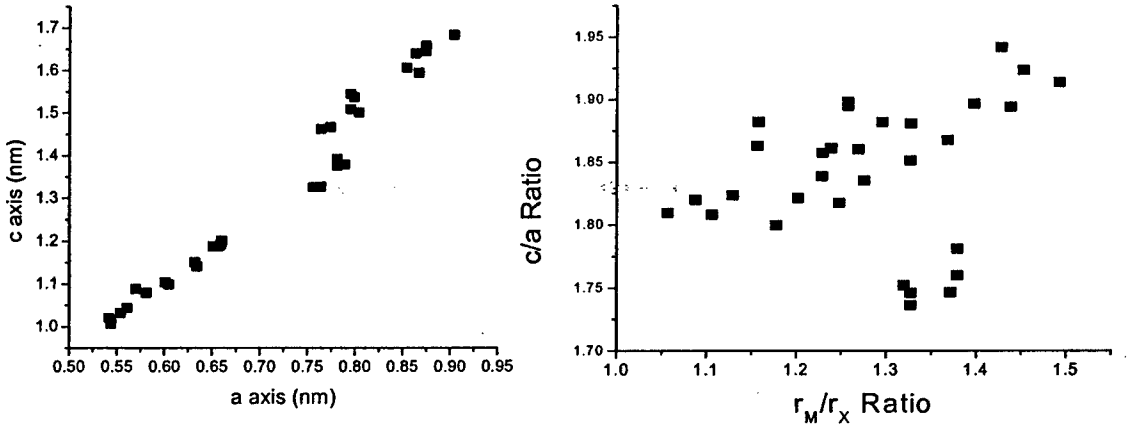

a) b)

FIGURE 22 Plot of a) lattice dimension of c and a from known T_2 compounds showing the restricted range of c/a (1.8 –1.9) and b) the atomic radius ratio versus the c/a for a wide range of observed T_2 phases

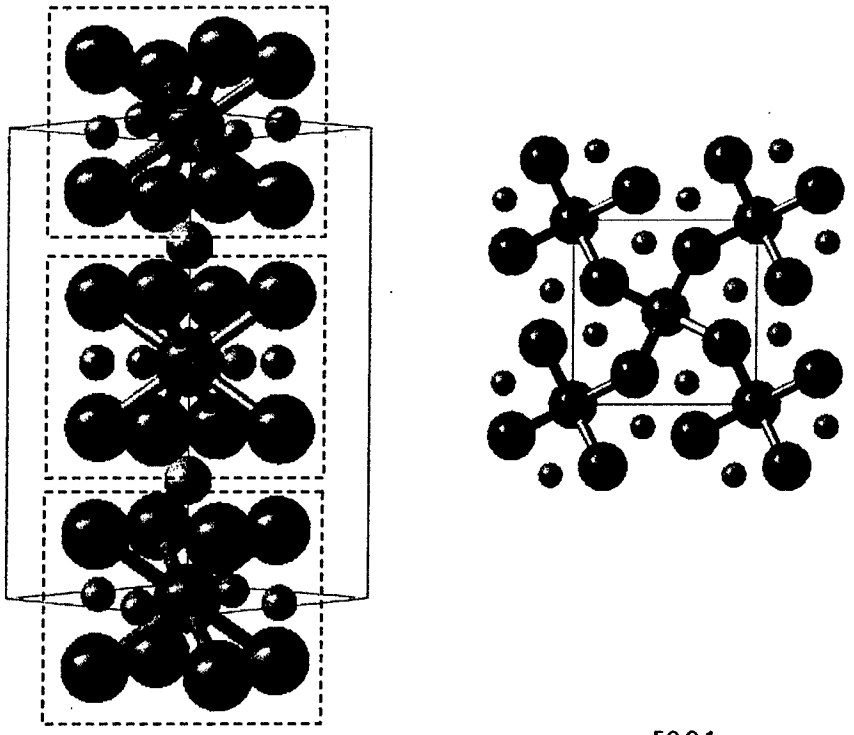

FIGURE 23 The Mo-Mo BCC-like clusters embedded in the T_2 tetragonal crystal surrounded by the Mo-Si and Mo-B polyhedra as shown from [110] and [001] directions. the contribution

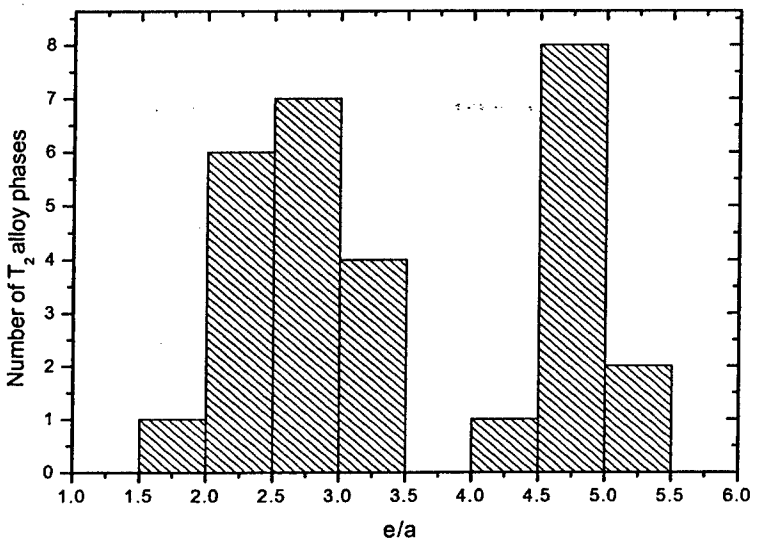

FIGURE 24 Plot of the occurrences of T_2 phases as a function of e/a showing two distinct groups

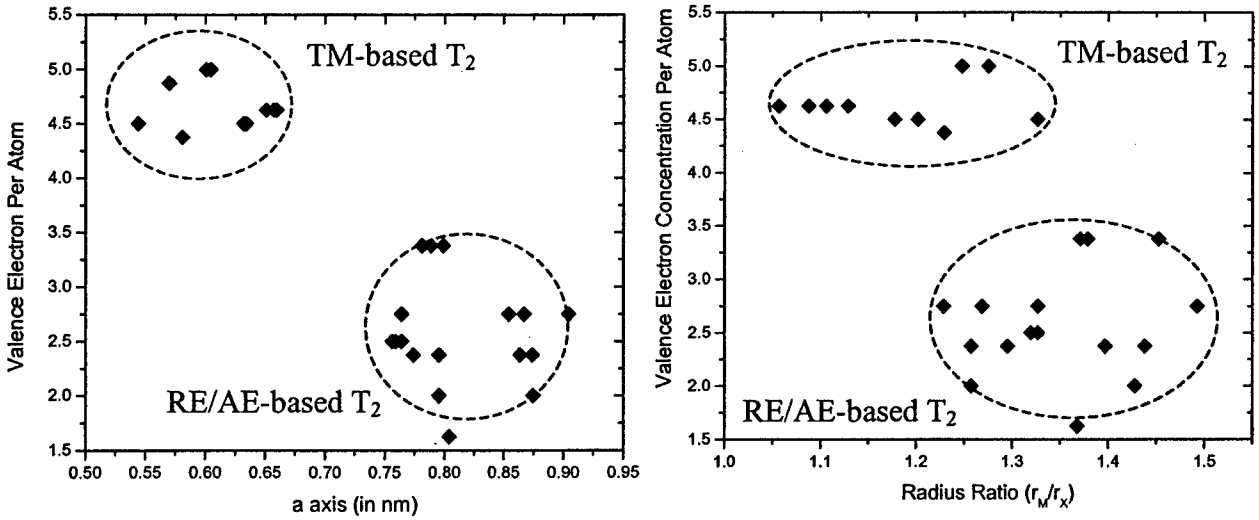

FIGURE 25 Plot of a) e/a versus lattice unit (a) and b) e/a versus atomic radius ratio. The two groups of T_2 phases also have different geometric characteristics; the low e/a, RE-based T_2 phase occurs with a relatively larger lattice unit cell and a higher radius ratio than that of the high e/a, TM-based T_2 phase.

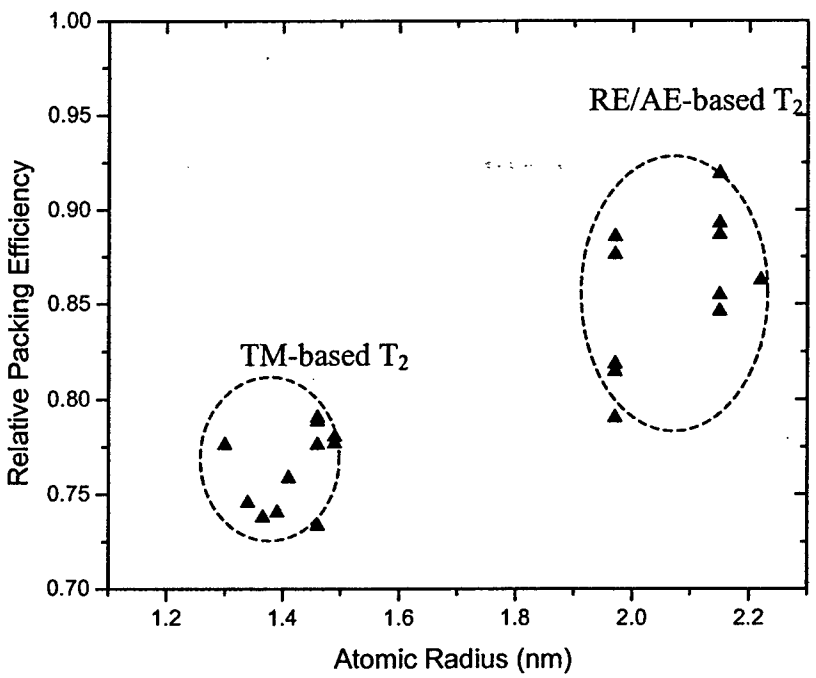

FIGURE 26 Plot of packing volume fraction of alloys with the T_2 phase structure showing the distinct grouping of the TM-based and RE-based T_2 phases.

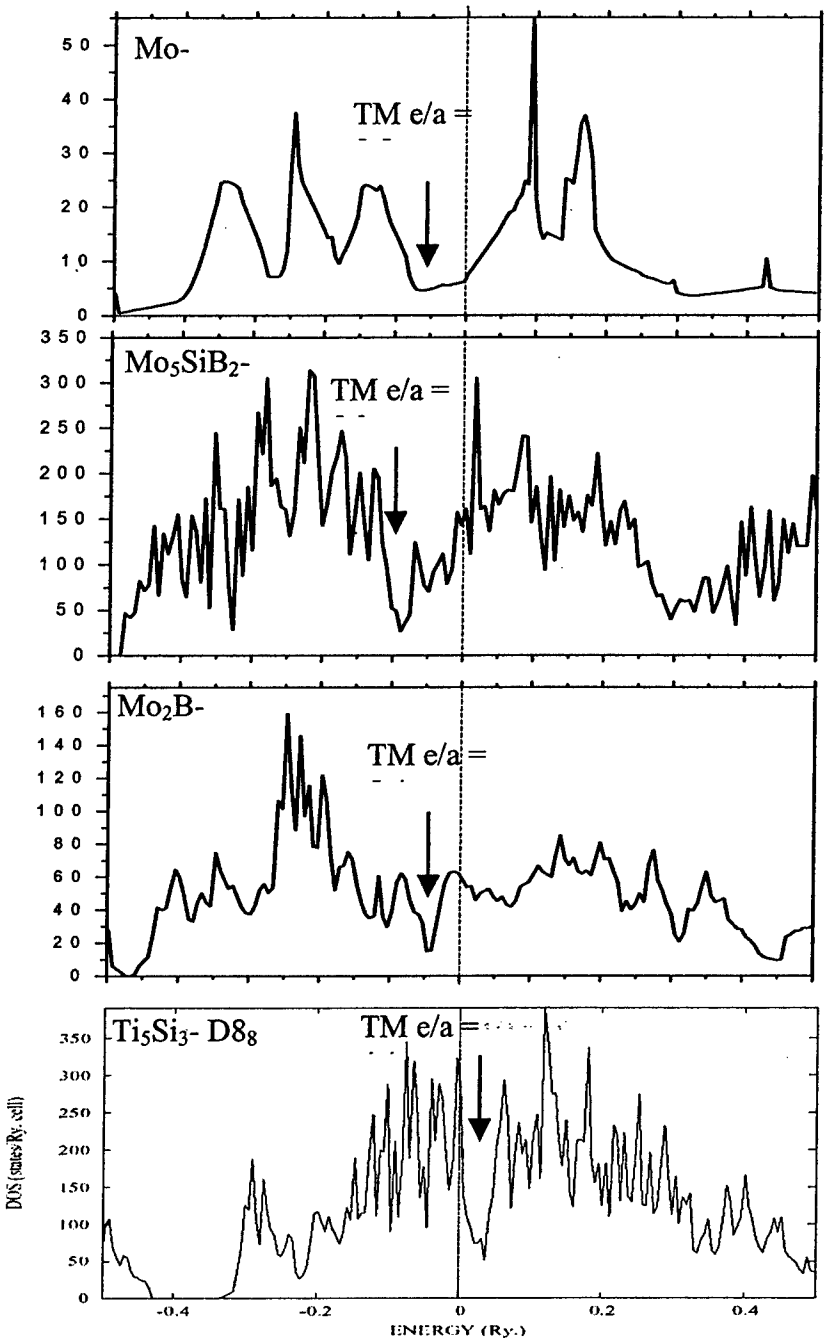

Figure 27: The Density of States of a) BCC, b) T_2, c) Mo_2B ($CuAl_2$-type) and d)$D8_8$ alloy structures with their respective optimum transition metal e/a for the minimum gap position (arrow). Note the low the optimum e/a for the $D8_8$ phase (4.2) which indicates as the phase is mostly stable with the Group IVB base metals. The scale in the x axes spans from 5 eV below and above the Fermi energy level that is placed at the origin.

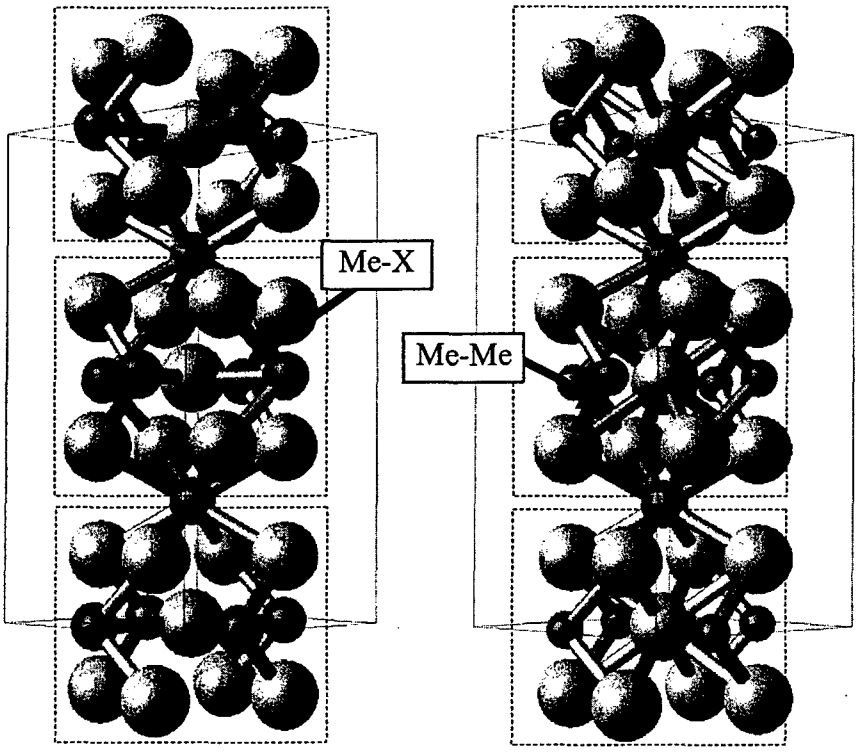

Figure 28 Clustering within the T_2 phase dominated by metal-metalloid contact only for the low e/a T_2 phase. Both metal-metal and metal-metalloid contact develop for the high e/a T_2 phase

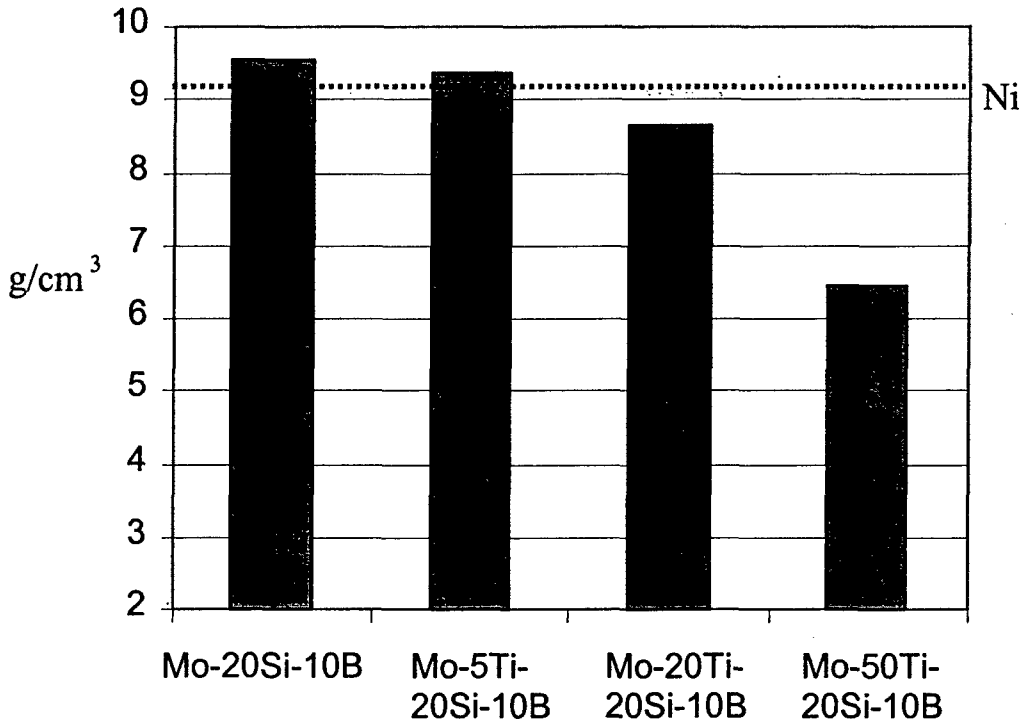

Figure 29 The effect of Ti substitution for Mo on the weight density.